

# Numerical modelling of ice sheets and ice shelves

Frank PATTYN\*

Laboratoire de Glaciologie, Université libre de Bruxelles, Brussels,  
Belgium

**Karthaus Summer School 2023**

## Contents

<b>1</b>	<b>Introduction</b>	<b>3</b>
<b>2</b>	<b>Commonly used approximations in ice flow modelling</b>	<b>4</b>
2.1	Stokes equations . . . . .	4
2.1.1	Field equations . . . . .	4
2.1.2	Constitutive equations . . . . .	5
2.1.3	Boundary conditions . . . . .	6
2.1.4	Approximations to the Stokes equations (FS) . . . . .	7
2.2	The Blatter–Pattyn model (LMLa) . . . . .	7
2.3	Shallow shelf approximation (SSA or L1L1) . . . . .	9
2.4	Shallow ice approximation (SIA or S) . . . . .	10
2.5	Hybrid models . . . . .	13
2.5.1	Classification of membrane stress fields . . . . .	13
2.5.2	L1L2 models . . . . .	13
2.5.3	L1L1* models . . . . .	14
2.6	Ice-sheet evolution . . . . .	15
2.7	Applicability of approximations . . . . .	15
<b>3</b>	<b>Numerical modelling of ice sheets and glaciers (SIA)</b>	<b>19</b>
3.1	Numerical methods . . . . .	19
3.1.1	FTCS scheme . . . . .	19
3.1.2	Numerical solution to a diffusive equation . . . . .	19
3.1.3	Numerical solution to an advection equation . . . . .	21
3.2	Explicit numerical solution for the ice-sheet equation . . . . .	22
3.3	Semi-implicit numerical solution of the ice-sheet equation . . . . .	24

---

\*Frank.Pattyn@ulb.be

3.4	Verification of SIA solutions . . . . .	28
3.4.1	The Nye-Vialov analytical solution . . . . .	28
3.5	Two-dimensional ice-sheet model . . . . .	28
3.5.1	Implicit time-stepping with a staggered grid . . . . .	30
3.5.2	A digression about sparse matrices . . . . .	33
3.6	EISMINT experiments . . . . .	36
3.7	A Greenland SIA ice sheet model . . . . .	36
<b>4</b>	<b>Numerical modelling of ice shelves and ice streams (SSA)</b>	<b>39</b>
4.1	Basic equations . . . . .	39
4.2	Boundary conditions . . . . .	40
4.2.1	Kinematic conditions . . . . .	40
4.2.2	Dynamic conditions . . . . .	40
4.2.3	Dynamic condition if $n = n_x$ . . . . .	41
4.3	Numerical solution of the SSA equations . . . . .	42
4.4	Example of an ice-shelf model . . . . .	42
<b>5</b>	<b>Numerical modelling of marine ice sheets</b>	<b>43</b>
5.1	Marine ice-sheet instability . . . . .	43
5.2	Schoof's boundary layer theory . . . . .	47
5.3	A flowline ice-stream SSA model with grounding line . . . . .	48
5.4	Numerical solution to the ice-stream model . . . . .	49
5.4.1	Velocity field . . . . .	49
5.4.2	Continuity equation . . . . .	50
5.4.3	Example . . . . .	51
5.5	MISMIP experiments . . . . .	51
5.6	Evaluating the buttressing effect of ice shelves . . . . .	53
<b>6</b>	<b>Conclusions</b>	<b>54</b>
	<b>Acknowledgments</b>	<b>55</b>
	<b>References</b>	<b>55</b>

# 1 Introduction

In order to understand the behaviour of glaciers and ice sheets in response to climatic changes over short and long time scales, ice sheet/glacier models are applied that comprise the principle mechanisms driving ice evolution. Although such models are simplified representations of the reality, they allow an assessment of past and future ice sheet evolution on a physical basis. The applicability of a specific model mainly depends on the included processes and the studied ice geometry. With the aim to better represent the real system, ice sheet models are continuously refined to include the most appropriate descriptions of the central physical processes. The most comprehensive ice sheet models are three-dimensional thermo-mechanically coupled ice sheet models that comprise three main components, describing the ice flow, the isostatic adjustment of the lithosphere and the mass balance at the upper and lower ice sheet boundaries. Marine ice sheet models also take into account the marine boundary (ice shelves and the interaction with the ocean). All these components interact either directly or indirectly by means of three evolution equations for ice thickness, bedrock and ice temperature, while accounting for mass and energy conservation. Local ice thickness changes are caused by surface and basal mass balance but also by divergent or convergent ice flow. The gravity-driven ice flow closes the system by linking interior regions of surface mass gain to the margin regions where mass loss is concentrated. Effects from isostatic adjustment cause additional uplift or subsidence of the ice body. Atmospheric temperature conditions over the ice sheet and geothermal heating from beneath set the boundary conditions for the internal ice temperature evolution.

Unlike atmospheric modelling, continental-scale ice-sheet modelling only fully emerged at the beginning of the 1990s (e.g., Huybrechts, 1990a; Huybrechts and Oerlemans, 1990). Initially, such models were employed at rather coarse resolution ( $\sim 50$  km) to investigate ice-sheet changes during glacial-interglacial cycles (Huybrechts, 1990b; Ritz et al, 2001) or on longer time scales (DeConto and Pollard, 2003). At that time, ice sheets were believed to be a slow component of the climate system with a highly diffusive response to surface mass balance change. However, while the possibility of rapid continental change was advocated several decades before (Weertman, 1974; Mercer, 1978), ice-sheet models were unable to deal with rapid changes, which was clearly identified as a limitation for Antarctic ice-sheet modelling (Vieli and Payne, 2005).

Due to the increase of satellite data observations witnessing rapid mass loss, ice-sheet modelling needed a paradigm shift, which came through an improved insight into grounding-line (limit between the grounded ice sheet and the floating ice shelf) physics and the way to represent this in ice-sheet models (Hindmarsh and Le Meur, 2001; Vieli and Payne, 2005; Pattyn et al, 2006; Schoof, 2007). Since then, ice-sheet modelling has taken a great leap forward based on an improved understanding of key processes and the development of assimilation methods leading to the ability to reproduce observed ice-sheet changes and by making refined future projections (Pattyn, 2018).

This course will focus on only one of these components, namely the evolution of ice sheets due to the deformation of ice. We will establish approximations to the general Stokes equations governing the flow of ice, derive the boundary conditions based on mass conservation and construct a simple ice sheet/glacier model. We will furthermore look into the dynamics of ice streams and derive an ice stream/ice shelf model, thereby producing and testing numerical codes that work. Finally, a more comprehensive insight in

marine ice sheet dynamics will be given, with a focus on grounding lines. The aim of the course is to construct numerical ice sheet and glacier models as a tool for investigating ice-sheet response at different time scales.

## 2 Commonly used approximations in ice flow modelling

### 2.1 Stokes equations

The Stokes equations approximate the Navier-Stokes equations for fluid flow, by neglecting momentum advection and inertia terms. Despite these approximations, the flow of ice is in a sense more complicated than the flow of air or water because it is not a Newtonian fluid. In other words, there is a non-linear relationship between the applied stress and the resulting strain rates. Deriving the Stokes equations requires a series of equations that relate conservation laws to the mechanical and thermal properties of the material. These are the conservation of mass, momentum and energy, known as the field equations. In order to link them, they are substituted into the field equations to obtain a system of numerically solvable equations, which is demonstrated below.

#### 2.1.1 Field equations

Conservation of mass is described by the continuity equation,

$$\frac{d\rho}{dt} + \nabla \cdot (\mathbf{v}\rho) = 0 \quad (2.1)$$

where  $\rho$  is the density and  $\mathbf{v}$  is the velocity vector. Considering ice as an incompressible material ( $\rho = \text{constant}$ ), this can be reduced to the incompressibility condition,

$$\nabla \cdot \mathbf{v} = 0 \quad (2.2)$$

Conservation of linear momentum is defined as:

$$\rho \frac{d\mathbf{v}}{dt} = \nabla \cdot \boldsymbol{\sigma} - \rho \mathbf{g} \quad (2.3)$$

where  $\boldsymbol{\sigma}$  is the Cauchy stress tensor and  $|\mathbf{g}| = 9.81 \text{ m s}^{-2}$  is the gravitational acceleration. For an ice sheet, the acceleration term (left hand side of 2.3) and the Coriolis force can be safely neglected. For a constant ice density, the momentum balance can be rewritten as

$$\nabla \cdot \boldsymbol{\sigma} + \rho_i \mathbf{g} = 0 \quad (2.4)$$

where  $\rho_i = 910 \text{ kg m}^{-3}$  is the density of ice. The conservation of angular momentum ensures that the Cauchy tensor is symmetric, i.e.  $\boldsymbol{\sigma} - \boldsymbol{\sigma}^T = 0$ , where  $\boldsymbol{\sigma}^T$  is the transpose of  $\boldsymbol{\sigma}$ . The final field equation is conservation of energy, which solves the thermodynamics of the ice. While this is also an essential part of ice sheet dynamics, it will not be treated in this course.

### 2.1.2 Constitutive equations

In order to solve the field equations, a constitutive equation is required, which is the material law equation that relates stress to strain. Glacier ice is a polycrystalline fluid with a stress-dependent viscosity. Due to its structure, there is a non-linear relationship between the applied stress and the resulting deformation, which can be expressed through Glen's flow law. Stress and deformation rates (represented by the strain tensor  $\dot{\epsilon}$ ) are assumed to follow a power law with a proportionality factor that depends on the ice rheology, which in turn depends on local ice temperature, i.e.,

$$\dot{\epsilon} = A\sigma_e^{n-1}\tau \quad (2.5)$$

where  $\tau$  is the deviatoric stress tensor, which are those stresses remaining once the hydrostatic stresses  $p\mathbf{I}$  are removed from  $\sigma$ ,

$$\tau = \sigma + p\mathbf{I} \quad (2.6)$$

where

$$p = -\frac{1}{3}\text{tr}\sigma \quad (2.7)$$

Since ice is considered incompressible, deformation does not depend on the total stress, but the deviation from the isotropic pressure  $p$  (defined positive when compressed).  $\sigma_e$  is the effective stress, defined as the second invariant of the stress tensor  $\sigma_e$  and defined by (making use of the Einstein summation convention)  $\sigma_e^2 = \frac{1}{2} \sum \tau_{ij}\tau_{ji}$ , or written in terms of tensor components,

$$2\sigma_e^2 = \tau_{xx}^2 + \tau_{yy}^2 + \tau_{zz}^2 + 2(\tau_{xy}^2 + \tau_{xz}^2 + \tau_{yz}^2) \quad (2.8)$$

$A$  is the temperature-dependent rate factor that obeys an Arrhenius law and may vary over several orders of magnitude within an ice sheet. This is the reason why modelling large ice sheets requires thermomechanical coupling and solving conservation of energy. For simplicity, rather than accuracy, we will continue with a constant value for  $A$ . The power law exponent  $n$  is generally assigned a value of 3, which is valid for large-scale flow, but may locally vary between 2–5 (especially close to ice divides, see Sect. 2.7). For application of this flow relation in the momentum equation, it is required that  $\tau$  is a function of  $\dot{\epsilon}$ . For this purpose, the inverse of Glen's flow law is used,

$$\tau = 2\eta\dot{\epsilon} \quad (2.9)$$

where  $\eta$  is the effective viscosity of the ice, which is strain-dependent due to the non-linear nature of the flow law,

$$\eta = \frac{1}{2}A^{-1/n}\dot{\epsilon}_e^{(1-n)/n} \quad (2.10)$$

where  $\dot{\epsilon}_e$  is the effective strain rate, defined as the second invariant of  $\dot{\epsilon}$ , i.e.,  $\dot{\epsilon}^2 = \frac{1}{2} \sum \dot{\epsilon}_{ij}\dot{\epsilon}_{ji}$ . The components of  $\dot{\epsilon}$  are defined as,

$$\dot{\epsilon}_{ij} = \frac{1}{2} \left( \frac{\partial v_i}{\partial x_j} + \frac{\partial v_j}{\partial x_i} \right) \quad (2.11)$$

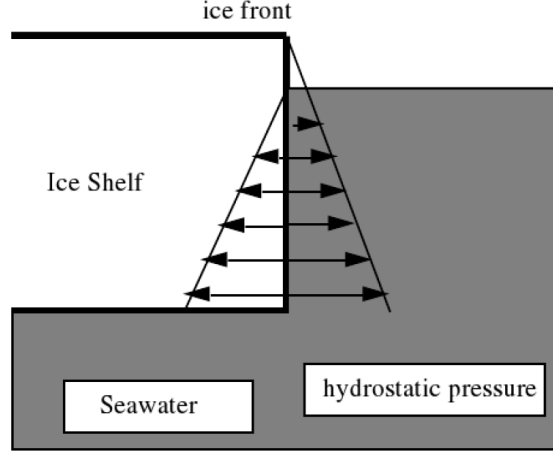


Figure 1: Force balance at an ice front which determines the dynamic boundary condition on an ice shelf.

Substituting (2.9) into the simplified momentum balance equation (2.4), results in the equation of motion,

$$-\nabla p + \nabla \cdot [\eta (\nabla \mathbf{v} + (\nabla \mathbf{v})^T)] + \rho_i \mathbf{g} = 0 \quad (2.12)$$

### 2.1.3 Boundary conditions

To close the system of equations, boundary conditions need to be defined for the various surfaces of the ice sheet. At the upper surface of the ice sheet  $s$  a stress free conditions is assumed,

$$\boldsymbol{\sigma} \cdot \mathbf{n} = 0 \quad (2.13)$$

where  $\mathbf{n}$  is the outward-pointing unit normal vector. This is the dynamic boundary condition for the free surface. At the base of the ice sheet, basal traction  $\boldsymbol{\tau}_b$  is the tangential component of the stress vector at the bed  $\boldsymbol{\sigma}|_{z=b}$ ,

$$\boldsymbol{\tau}_b = \begin{cases} -C|\mathbf{v}_b|^{m-1}\mathbf{v}_b & h \frac{\rho_i}{\rho_w} > -b \\ 0 & \text{otherwise} \end{cases} \quad (2.14)$$

where  $h$  is the ice thickness,  $b$  the bedrock elevation, and  $\rho_w$  the density of seawater. Basal traction is zero when the ice sheet starts to get afloat and forms an ice shelf.  $\boldsymbol{\tau}_b$  follows a sliding law where the ice grounded on bedrock, with  $C$  and  $m$  being parameters of the sliding law. The velocity outwardly normal to the the base is zero where ice is in contact with the bedrock, i.e.  $\mathbf{v} \cdot \mathbf{n} = 0$ . If the ice is in contact with water (such as an ice shelf), then water pressure is applied to the ice-water interface (Fig. 1),

$$\boldsymbol{\sigma} \cdot \mathbf{n} = \rho_w g z \mathbf{n} \quad (2.15)$$

A detailed derivation of this shelf front boundary conditions is given in Sect. 4.

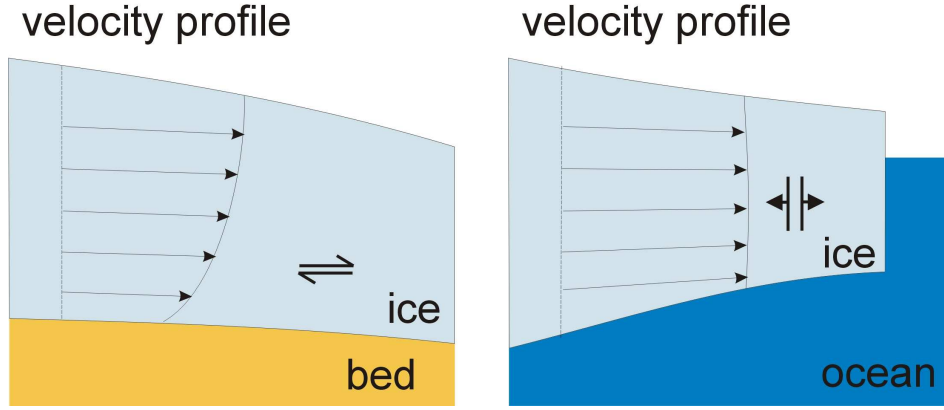


Figure 2: Ice flow within a grounded ice sheet (left) and within a floating ice shelf (right)

#### 2.1.4 Approximations to the Stokes equations (FS)

Models that solve the above system of equations are called full-Stokes models. They represent the most complete mathematical description of ice sheet dynamics. However, solving them requires great amounts of computational power, so that they are applied on specific glaciers or parts of ice sheets. Therefore, many models use approximations of the full-Stokes system. The approximations take advantage of the aspect ratio of ice sheets (e.g. the fact that ice sheet thickness is very small compared to the horizontal extent), allowing terms to be neglected in the momentum balance equations. Simplifications are also required for the constitutive equations and boundary conditions. To illustrate the major differences in ice-flow types we may consider the dominant deformational process in glaciers/ice sheets and ice stream/ice shelves: glaciers lie on sloping bedrock and gravity ‘pulls’ a glacier to the center of the Earth. Ice sheets spread under their own weight. Their dominant deformational process (in the absence of sliding) is shearing in the vertical (Fig. 2). Ice shelves are buoyant, ice wants to spread—like a drop of oil on water. Their deformational behaviour is determined by longitudinal stretching (Fig. 2). Therefore, approximations to the Stokes equations will also depend on the type of ice flow.

In order to make the simplifications to the momentum balance, we can rewrite the balance equation in its component form, as shown in Fig. 3,

$$\frac{\partial \tau_{xx}}{\partial x} + \frac{\partial \tau_{xy}}{\partial y} + \frac{\partial \tau_{xz}}{\partial z} = \frac{\partial p}{\partial x} \quad (2.16)$$

$$\frac{\partial \tau_{xy}}{\partial x} + \frac{\partial \tau_{yy}}{\partial y} + \frac{\partial \tau_{yz}}{\partial z} = \frac{\partial p}{\partial y} \quad (2.17)$$

$$\frac{\partial \tau_{xz}}{\partial x} + \frac{\partial \tau_{yz}}{\partial y} + \frac{\partial \tau_{zz}}{\partial z} = \frac{\partial p}{\partial z} + \rho_i g \quad (2.18)$$

## 2.2 The Blatter–Pattyn model (LMLa)

Below the full-Stokes model in the hierarchy of approximations sits the so-called Blatter–Pattyn model, or sometimes referred to as first-order or higher-order model. This type of

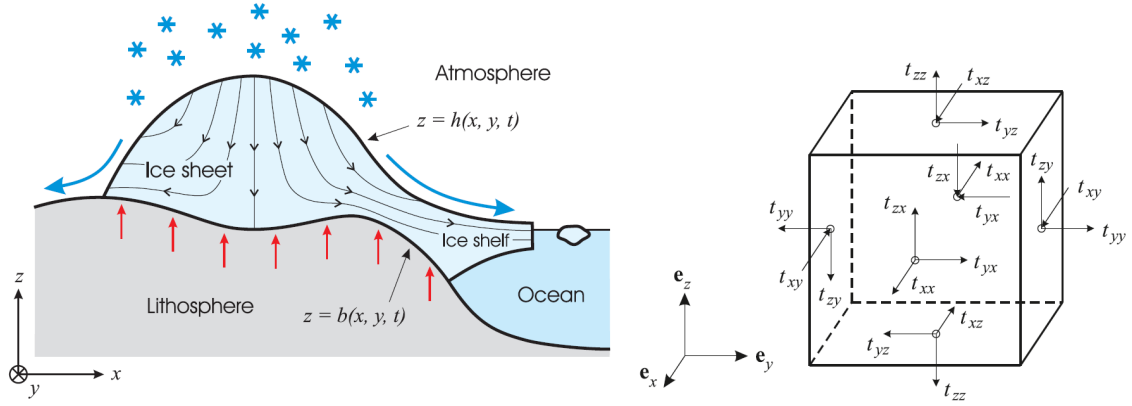


Figure 3: Coordinate system for the ice sheet model (left); momentum balance (right)

model simplifies the full-Stokes equations by making two assumptions. The first assumption is the hydrostatic assumption in the vertical direction, stating that shear stresses are small compared to the vertical normal stress,

$$\frac{\partial \tau_{xz}}{\partial x}, \frac{\partial \tau_{yz}}{\partial y} \ll \frac{\partial \tau_{zz}}{\partial z} \quad (2.19)$$

so that the vertical momentum balance (2.18) can be reduced to

$$\frac{\partial \tau_{zz}}{\partial z} = \frac{\partial p}{\partial z} + \rho_i g \quad (2.20)$$

Integration over the vertical leads to an explicit expression for  $p$ . Neglecting atmospheric pressure, i.e.  $p(s) = 0$ , this leads to,

$$p = \tau_{zz}(z) + \rho_i g(s - z) \quad (2.21)$$

which means that the vertical normal stresses are balanced by the hydrostatic pressure. This can be used to eliminate pressure from the momentum balance equations:

$$\frac{\partial \tau_{xx}}{\partial x} - \frac{\partial \tau_{zz}}{\partial x} + \frac{\partial \tau_{xy}}{\partial y} + \frac{\partial \tau_{xz}}{\partial z} = \rho_i g \frac{\partial s}{\partial x} \quad (2.22)$$

$$\frac{\partial \tau_{yy}}{\partial y} - \frac{\partial \tau_{zz}}{\partial y} + \frac{\partial \tau_{xy}}{\partial x} + \frac{\partial \tau_{yz}}{\partial z} = \rho_i g \frac{\partial s}{\partial y} \quad (2.23)$$

Due to the incompressibility condition,  $\tau_{zz} = -\tau_{xx} - \tau_{yy}$ , terms including the vertical normal deviatoric stress  $\tau_{zz}$  are written in terms of horizontal normal deviatoric stresses,

$$2 \frac{\partial \tau_{xx}}{\partial x} + \frac{\partial \tau_{yy}}{\partial x} + \frac{\partial \tau_{xy}}{\partial y} + \frac{\partial \tau_{xz}}{\partial z} = \rho_i g \frac{\partial s}{\partial x} \quad (2.24)$$

$$2 \frac{\partial \tau_{yy}}{\partial y} + \frac{\partial \tau_{xx}}{\partial y} + \frac{\partial \tau_{xy}}{\partial x} + \frac{\partial \tau_{yz}}{\partial z} = \rho_i g \frac{\partial s}{\partial y} \quad (2.25)$$

The hydrostatic approximation is the basis for all approximations for ice flow. It allows to eliminate one of the four unknowns, namely pressure  $p$  from the stress balance.



Eqs. 2.24 and 2.25 are then written in terms of velocity components ( $u, v, w$ ) by using the constitutive equation for the stress-strain relationship (2.9) and (2.11),

$$\frac{\partial}{\partial x} \left( 4\eta \frac{\partial u}{\partial x} + 2\eta \frac{\partial v}{\partial y} \right) + \frac{\partial}{\partial y} \left( \eta \frac{\partial u}{\partial y} + \eta \frac{\partial v}{\partial x} \right) + \frac{\partial}{\partial z} \left( \eta \frac{\partial u}{\partial z} + \eta \frac{\partial w}{\partial x} \right) = \rho_i g \frac{\partial s}{\partial x} \quad (2.26)$$

$$\frac{\partial}{\partial y} \left( 4\eta \frac{\partial v}{\partial y} + 2\eta \frac{\partial u}{\partial x} \right) + \frac{\partial}{\partial x} \left( \eta \frac{\partial v}{\partial x} + \eta \frac{\partial u}{\partial y} \right) + \frac{\partial}{\partial z} \left( \eta \frac{\partial v}{\partial z} + \eta \frac{\partial w}{\partial y} \right) = \rho_i g \frac{\partial s}{\partial y} \quad (2.27)$$

Further terms can be eliminated based on the aspect ratios of ice sheets. This forms the second assumption made in Blatter-Pattyn models. If the ratio of typical values of the velocity and extents are considered, it is easy to see that the horizontal derivatives of the vertical velocity component are negligible compared to the vertical derivatives of the horizontal velocity,

$$\frac{\frac{\partial w}{\partial x}}{\frac{\partial u}{\partial z}}, \frac{\frac{\partial w}{\partial y}}{\frac{\partial v}{\partial z}} \sim \frac{\frac{0.1 \text{ m a}^{-1}}{10^6 \text{ m}}}{\frac{100 \text{ m a}^{-1}}{1000 \text{ m}}} = 10^{-6} \quad (2.28)$$

Therefore the  $\frac{\partial w}{\partial x}$  and  $\frac{\partial w}{\partial y}$  terms may be safely neglected, so that,

$$\frac{\partial}{\partial x} \left( 4\eta \frac{\partial u}{\partial x} + 2\eta \frac{\partial v}{\partial y} \right) + \frac{\partial}{\partial y} \left( \eta \frac{\partial u}{\partial y} + \eta \frac{\partial v}{\partial x} \right) + \frac{\partial}{\partial z} \left( \eta \frac{\partial u}{\partial z} \right) = \rho_i g \frac{\partial s}{\partial x} \quad (2.29)$$

$$\frac{\partial}{\partial y} \left( 4\eta \frac{\partial v}{\partial y} + 2\eta \frac{\partial u}{\partial x} \right) + \frac{\partial}{\partial x} \left( \eta \frac{\partial v}{\partial x} + \eta \frac{\partial u}{\partial y} \right) + \frac{\partial}{\partial z} \left( \eta \frac{\partial v}{\partial z} \right) = \rho_i g \frac{\partial s}{\partial y} \quad (2.30)$$

The Blatter-Pattyn model, like the full-Stokes model is still three-dimensional in terms of horizontal velocity, but by neglecting vertical resistive stresses the resulting model is faster than the full-Stokes model, partly because the number of degrees of freedom is halved (from  $p, u, v, w$  to  $u, v$ ) and partly because pressure is given by a simple formula. The resulting system can be easily solved through iteration (see Sect. 4).

### 2.3 Shallow shelf approximation (SSA or L1L1)

The shallow shelf approximation (SSA) is a further approximation to the Blatter-Pattyn approximation, by besides the hydrostatic approximation further neglecting vertical shear stresses. In ice streams and ice shelves, the basal sliding is greater than the vertical shear, and together with horizontal, longitudinal and lateral stretching (or membrane stresses), dominates the stress balance. These membrane stresses are non-local, meaning that the driving stress is balanced by stretching ice that is at a distance away. The momentum balance equations become,

$$\frac{\partial \tau_{xx}}{\partial x} + \frac{\partial \tau_{xy}}{\partial y} = \frac{\partial p}{\partial x} \quad (2.31)$$

$$\frac{\partial \tau_{xy}}{\partial x} + \frac{\partial \tau_{yy}}{\partial y} = \frac{\partial p}{\partial y} \quad (2.32)$$

$$\frac{\partial \tau_{zz}}{\partial z} = \frac{\partial p}{\partial z} + \rho_i g \quad (2.33)$$

This assumption automatically reduces the model to the hydrostatic approximation as seen with the Blatter-Pattyn model. Therefore, pressure can be eliminated and the vertical deviatoric stresses can be written in terms of the horizontal normal deviatoric stresses,

$$2\frac{\partial\tau_{xx}}{\partial x} + \frac{\partial\tau_{yy}}{\partial x} + \frac{\partial\tau_{xy}}{\partial y} = \rho_i g \frac{\partial s}{\partial x} \quad (2.34)$$

$$2\frac{\partial\tau_{yy}}{\partial y} + \frac{\partial\tau_{xx}}{\partial y} + \frac{\partial\tau_{xy}}{\partial x} = \rho_i g \frac{\partial s}{\partial y} \quad (2.35)$$

This pair of equations can be integrated in the vertical to give them in terms of vertically-integrated variables,

$$\frac{\partial}{\partial x} \left( 2\eta h \left( 2\frac{\partial u}{\partial x} + \frac{\partial v}{\partial y} \right) \right) + \frac{\partial}{\partial y} \left( \eta h \left( \frac{\partial u}{\partial y} + \frac{\partial v}{\partial x} \right) \right) = \rho_i g h \frac{\partial s}{\partial x} \quad (2.36)$$

$$\frac{\partial}{\partial y} \left( 2\eta h \left( 2\frac{\partial v}{\partial y} + \frac{\partial u}{\partial x} \right) \right) + \frac{\partial}{\partial x} \left( \eta h \left( \frac{\partial v}{\partial x} + \frac{\partial u}{\partial y} \right) \right) = \rho_i g h \frac{\partial s}{\partial y} \quad (2.37)$$

SSA reduces the problem to a two-dimensional elliptic one, which is advantageous in terms of computational cost over the three-dimensional Blatter-Pattyn and full-Stokes models. The approximation applies well for large ice shelves, in regions away from the calving front and grounding lines. With the addition of a basal traction term, they also are capable of modelling ice streams, as long as the ice stream has a weak bed strength and is across relatively smooth bed topography. The equations then become,

$$\frac{\partial}{\partial x} \left( 2\eta h \left( 2\frac{\partial u}{\partial x} + \frac{\partial v}{\partial y} \right) \right) + \frac{\partial}{\partial y} \left( \eta h \left( \frac{\partial u}{\partial y} + \frac{\partial v}{\partial x} \right) \right) - \beta^2 u = \rho_i g h \frac{\partial s}{\partial x} \quad (2.38)$$

$$\frac{\partial}{\partial y} \left( 2\eta h \left( 2\frac{\partial v}{\partial y} + \frac{\partial u}{\partial x} \right) \right) + \frac{\partial}{\partial x} \left( \eta h \left( \frac{\partial v}{\partial x} + \frac{\partial u}{\partial y} \right) \right) - \beta^2 v = \rho_i g h \frac{\partial s}{\partial y} \quad (2.39)$$

where  $\tau_b = \beta^2 \mathbf{v}$  is the basal drag and  $\beta^2$  a friction parameter that can be a function of velocity as a function of the friction law used. For ice shelves, the basal stress is set to zero, so that  $\beta^2 = 0$ , and so the driving stress of sully supported by membrane stresses. When the ice is fully frozen to the bed, membrane stresses account for very little of the driving stress and therefore SSA is not valid.

## 2.4 Shallow ice approximation (SIA or S)

The greatest simplification of the Stokes equations is the shallow ice approximation (SIA). This approximation is most widely used for large-scale simulations, owing to the fact that for the vast majority of an ice sheet the flow regime is dominated by shearing parallel to the bed (Fig. 2). Therefore, only the vertical gradients of the vertical shear stresses are of interest, while membrane stresses are neglected,

$$\frac{\partial \tau_{xz}}{\partial z} = \frac{\partial p}{\partial x} \quad (2.40)$$

$$\frac{\partial \tau_{yz}}{\partial z} = \frac{\partial p}{\partial y} \quad (2.41)$$

$$0 = \frac{\partial p}{\partial z} + \rho_i g \quad (2.42)$$

The body force  $\rho_i g$  is balanced by the vertical pressure gradient. Some excluded stresses may not be small compared to each other (e.g.  $\partial \tau_{xx}$  is comparable to  $\partial \tau_{xz}$ , but if the horizontal gradient  $dx$  is considered, they become insignificant due to the large horizontal length scales. Integrating the momentum balance equations from the surface  $s$  to a height  $z$  in the ice sheet,

$$\int_z^s \frac{\partial \tau_{xz}}{\partial z} dz = \int_z^s \frac{\partial p}{\partial x} dz \quad (2.43)$$

$$\int_z^s \frac{\partial \tau_{yz}}{\partial z} dz = \int_z^s \frac{\partial p}{\partial y} dz \quad (2.44)$$

$$p(s) - p(z) = \rho_i g(s - z) \quad (2.45)$$

with the stress-free condition at the surface this leads to

$$\tau_{xz}(z) = -\rho_i g(s - z) \frac{\partial s}{\partial x} \quad (2.46)$$

$$\tau_{yz}(z) = -\rho_i g(s - z) \frac{\partial s}{\partial y} \quad (2.47)$$

These equations show that the SIA stress field can be fully determined if the local geometry is known (surface elevation, ice thickness and surface slope). In contrast to the SSA, the locally defined ice mass is not affected by upstream or downstream ice (through membrane stresses). This state of stress is completely independent of ice rheology and the velocity can be calculated explicitly, rather than through a system of partial differential equations. Given the SIA, the effective stress is reduced to

$$\sigma_e = \sqrt{\tau_{xz}^2 + \tau_{yz}^2} \quad (2.48)$$

which with (2.46) and (2.47) leads to

$$\frac{\partial u}{\partial z} = -2A [\rho_i g(s - z)]^n |\nabla s|^{n-1} \frac{\partial s}{\partial x} \quad (2.49)$$

$$\frac{\partial v}{\partial z} = -2A [\rho_i g(s - z)]^n |\nabla s|^{n-1} \frac{\partial s}{\partial y} \quad (2.50)$$

The horizontal velocity field is determined by integrating (2.49) and (2.50) from the base of the ice sheet  $b$  to a height  $z$ :

$$u(z) - u(b) = -2A (\rho_i g)^n |\nabla s|^{n-1} \frac{\partial s}{\partial x} \int_b^z (s - z)^n dz \quad (2.51)$$

$$v(z) - v(b) = -2A (\rho_i g)^n |\nabla s|^{n-1} \frac{\partial s}{\partial y} \int_b^z (s - z)^n dz \quad (2.52)$$

which leads to

$$u(z) - u(b) = \frac{2A}{n+1} (\rho_i g)^n |\nabla s|^{n-1} \frac{\partial s}{\partial x} [(s - z)^{n+1} - h^{n+1}] \quad (2.53)$$

$$v(z) - v(b) = \frac{2A}{n+1} (\rho_i g)^n |\nabla s|^{n-1} \frac{\partial s}{\partial y} [(s - z)^{n+1} - h^{n+1}] \quad (2.54)$$

The vertical mean horizontal velocity is obtained by integrating (2.53) and (2.54) once more from the base of the ice mass to the surface, divided over the ice thickness  $h$ , so that

$$\bar{u} - u(b) = \frac{2A}{(n+2)h} (\rho_i g)^n |\nabla s|^{n-1} \frac{\partial s}{\partial x} \int_b^s [(s - z)^{n+1} - h^{n+1}] dz \quad (2.55)$$

$$\bar{v} - v(b) = \frac{2A}{(n+2)h} (\rho_i g)^n |\nabla s|^{n-1} \frac{\partial s}{\partial y} \int_b^s [(s - z)^{n+1} - h^{n+1}] dz \quad (2.56)$$

which leads to

$$\bar{u} - u(b) = -\frac{2A}{n+2} (\rho_i g)^n |\nabla s|^{n-1} \frac{\partial s}{\partial x} h^{n+1} \quad (2.57)$$

$$\bar{v} - v(b) = -\frac{2A}{n+2} (\rho_i g)^n |\nabla s|^{n-1} \frac{\partial s}{\partial y} h^{n+1} \quad (2.58)$$

This can also be written as,

$$\bar{u} - u(b) = \frac{2A}{n+2} h |\tau_{dx}|^{n-1} \tau_{dx} \quad (2.59)$$

$$\bar{v} - v(b) = \frac{2A}{n+2} h |\tau_{dy}|^{n-1} \tau_{dy} \quad (2.60)$$

where  $\tau_{dx}$  is the driving stress in the  $x$  direction defined by  $\tau_{dx} = -\rho g h \frac{\partial s}{\partial x}$  (idem for  $\tau_{dy}$ ). Note, however, that we considered the flow factor in Glen's flow law  $A$  to be constant for the ice sheet, and therefore treated as a constant. In thermomechanical models,  $A$  should be properly integrated over the vertical.

## 2.5 Hybrid models

### 2.5.1 Classification of membrane stress fields

Hindmarsh (2004) developed a classification scheme for higher-order models based on the different “longitudinal stress schemes” widely used in ice sheet modelling. The most common longitudinal stress approximations introduce the two horizontal velocity components as field variables. This leads to an elliptic system with two rather than four variables of the full system at points in three-dimensional space (Pattyn, 2003; Hindmarsh, 2004), and the resulting linear systems are generally better conditioned than those resulting from the numerical analysis of the full system (Hindmarsh, 2004). These models are termed “multilayer models”. A number of these models solve an elliptic system at one elevation only (generally the upper surface), giving a computationally two-dimensional problem. These higher-order approximations are labelled L1L1, L1L2, LMLa, LTSML and L1L1\* (Hindmarsh, 2004). Models without membrane stresses, such as SIA, are labelled S.

The L1L1 approximation is a one-layer longitudinal stress scheme using  $\tau_{xx}$  at the surface computed by solving elliptic equations and is identical to the approximation used by Morland (1987) and MacAyeal (1989) and presented here as SSA. An alternative approximation is the L1L2 approach, or one-layer longitudinal stress scheme, using  $\dot{\epsilon}_{xx}$  at the surface computed by solving elliptical equations with a vertical correction of  $\tau_{xx}$ . Here, the surface velocities used in computing the non-horizontal plane stresses are computed using the vertical shear stresses in the shear strain relationship and in the sliding relationship.

The most common approximation is the LMLa or multilayer longitudinal stress scheme. This is the classic longitudinal stress scheme used by Blatter (1995) and Pattyn (2003). Compared with L1L2, the longitudinal stresses use the velocity at the corresponding elevations rather than at the surface, and the stress-invariant calculations are self-consistent rather than using the SIA stress (Hindmarsh, 2004). Finally, there is the LTSML or multilayer longitudinal stresses scheme with horizontal shear stress gradients approximated by SIA. Here, horizontal gradients of the vertical velocity are neglected. Horizontal plane shear stresses, when needed to calculate the horizontal gradient of such shear stresses, are approximated by SIA values. This approach is similar to LMLa, but with inclusion of the vertical resistive stress, as in Van der Veen and Whillans (1989).

### 2.5.2 L1L2 models

This is the so-called Schoof-Hindmarsh approach (Schoof and Hindmarsh, 2010) and implemented in e.g. the BISICLES model (Cornford et al, 2013). Compared to the SSA model, the second invariant of the deviatoric stress tensor takes also into account the vertical shear stresses, which are then approximated by the SIA model. The difference with the SSA model lies in the fact that a third degree polynomial equation has to be solved to compute the effective viscosity  $\eta$ . This equation is solved at different depths, and the final result is vertically integrated to compute the final effective viscosity.

The deviatoric stress tensor  $\tau$  is broken down as the sum of two matrices, one for the vertical shear stresses  $\phi$ , and one for the other stresses  $\psi$ ,

$$\begin{pmatrix} \tau_{xx} & \tau_{xy} & \tau_{xz} \\ \tau_{xy} & \tau_{yy} & \tau_{yz} \\ \tau_{xz} & \tau_{yz} & \tau_{zz} \end{pmatrix} = \begin{pmatrix} \tau_{xx} & \tau_{xy} & 0 \\ \tau_{xy} & \tau_{yy} & 0 \\ 0 & 0 & \tau_{zz} \end{pmatrix} + \begin{pmatrix} 0 & 0 & \tau_{xz} \\ 0 & 0 & \tau_{yz} \\ \tau_{xz} & \tau_{yz} & 0 \end{pmatrix} = \boldsymbol{\psi} + \boldsymbol{\phi} \quad (2.61)$$

where  $\tau_{xz} = -\rho_i g(s - z) \frac{\partial s}{\partial x}$  and  $\tau_{yz} = -\rho_i g(s - z) \frac{\partial s}{\partial y}$ , both determined from SIA. Considering the vertical shear stresses in the effective viscosity, but not in the stress tensor, Glen's flow law then becomes

$$\dot{\epsilon}_e = A \left( \psi_e^2 + \phi_e^2 \right)^{(n-1)/2} \boldsymbol{\psi} \quad (2.62)$$

where  $\psi_e$  is the second invariant of  $\boldsymbol{\psi}$ , and  $\phi_e$  is the second invariant of  $\boldsymbol{\psi}$ , given by the SIA as

$$\phi_e^2 = (\rho_i g(s - z))^2 \left[ \left( \frac{\partial s}{\partial x} \right)^2 + \left( \frac{\partial s}{\partial y} \right)^2 \right] \quad (2.63)$$

Assuming the inverse flow law as  $\boldsymbol{\psi} = 2\eta\dot{\epsilon}$ , we have  $\psi_e^2 = 4\eta^2\dot{\epsilon}_e^2$ , which, combined with (2.62) becomes,

$$\dot{\epsilon}_e = A \left( 4\eta^2\dot{\epsilon}_e^2 + \phi_e^2 \right)^{(n-1)/2} \boldsymbol{\psi} \quad (2.64)$$

In combination with the inverse flow law, this results in,

$$2\eta A \left( 4\eta^2\dot{\epsilon}_e^2 + \phi_e^2 \right) = 1 \quad (2.65)$$

### 2.5.3 L1L1\* models

This approximation consists of employing the SSA as a sliding law in an SIA model (Bueler and Brown, 2009). This means combining the velocities computed by SIA and SSA to get the velocity used in mass continuity and conservation of energy. Considering that  $\mathbf{u} = (u_x, u_y)$  is the SIA velocity and  $\mathbf{v} = (v_x, v_y)$  is the SSA velocity, we compute the combined horizontal velocity  $\mathbf{U} = (U_x, U_y)$  by

$$\mathbf{U} = f(|\mathbf{v}|) \mathbf{u} + (1 - f(|\mathbf{v}|)) \mathbf{v} \quad (2.66)$$

where  $|\mathbf{v}|^2 = v_x^2 + v_y^2$  and

$$f(|\mathbf{v}|) = 1 - \arctan \left( \frac{|\mathbf{v}|^2}{100^2} \right) \quad (2.67)$$

The weighting function  $f$  has values between zero and one. While this function guarantees a smooth combination between both SSA and SIA velocities, several authors simply combine both fields by addition, i.e.  $\mathbf{U} = \mathbf{u} + \mathbf{v}$  (Winkelmann et al, 2011; Pollard and DeConto, 2012; Pattyn, 2017).

## 2.6 Ice-sheet evolution

Mass conservation implies that

$$\frac{\partial u}{\partial x} + \frac{\partial v}{\partial y} + \frac{\partial w}{\partial z} = 0 \quad (2.68)$$

from which it follows that

$$w(s) - w(b) = - \int_b^s \nabla \cdot \mathbf{v}_H(z) dz \quad (2.69)$$

where  $\mathbf{v}_H$  are the components of the horizontal velocity ( $u, v$ ). At the upper and lower surfaces, respectively, kinematic boundary conditions apply, i.e.,

$$w(b) = \frac{\partial b}{\partial t} + \mathbf{v}_H(b) \cdot \nabla b - M_b \quad (2.70)$$

$$w(s) = \frac{\partial s}{\partial t} + \mathbf{v}_H(s) \cdot \nabla s - M_s \quad (2.71)$$

where  $M_s$  and  $M_b$  are the surface and basal mass balance, respectively. Using Leibniz integration rule, we obtain

$$w(s) - w(b) = -\nabla \cdot \int_b^s \mathbf{v}_H(z) dz + \mathbf{v}_H(s) \cdot \nabla s - \mathbf{v}_H(b) \cdot \nabla b \quad (2.72)$$

$$= -\nabla \cdot (\bar{\mathbf{v}}_H h) + \mathbf{v}_H(s) \cdot \nabla s - \mathbf{v}_H(b) \cdot \nabla b \quad (2.73)$$

In combination with the kinematic boundary conditions, this leads to

$$\frac{\partial h}{\partial t} = -\nabla \cdot (\bar{\mathbf{v}}_H h) + M_s - M_b \quad (2.74)$$

This is the main equation to solve, which is documented in Sect. 3.

## 2.7 Applicability of approximations

The SIA is valid for all regions in ice sheets characterized by slow moving ice (generally  $<100 \text{ m a}^{-1}$ ) with limited basal sliding. Exceptions are ice divides and grounding lines (or transition zones between the grounded ice sheet and the floating ice shelf). Fig. 4 distinguishes between the different flow types, where clearly fast flowing features can be observed penetrating far into the ice sheet. Here, SIA is not valid and membrane stresses need to be taken into account.

Ice divides are a separate case, since due to the absence of vertical shearing, membrane stresses operate in a dominant way within a few ice thicknesses from the ice divide. For large scale ice-sheet modelling, this is not such a big deal, since horizontal grid spacing is generally tens of ‘ice thicknesses’. Indeed, at ice divides the so-called Raymond effect operates (Raymond, 1983). Due to the nonlinear flow law, ice underneath the ice divide is stiffer than away from it, because of the fact that strain enhancement is lacking in the absence of vertical shearing. As a consequence, isochronous layers within the ice sheet are draped over stiffer ice underneath the divide, resulting in apparent isochronous arches in radargrams (Fig. 5, from Drews et al (2015)).

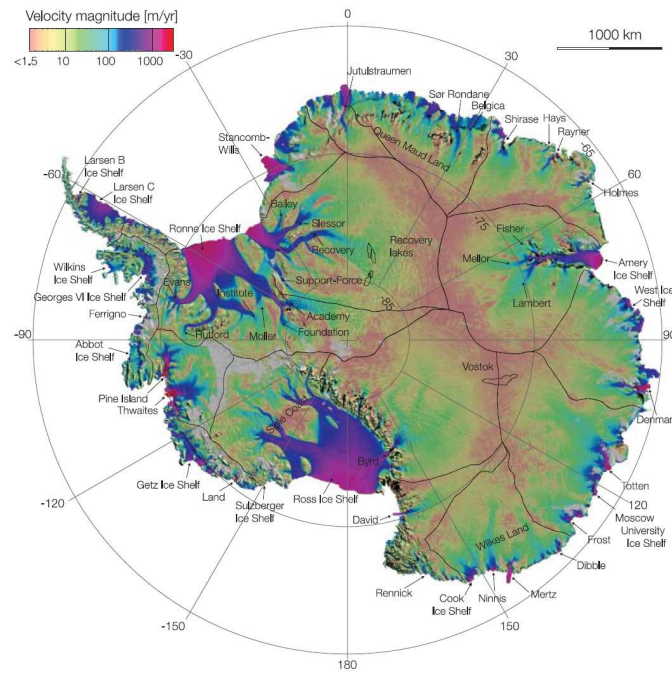


Figure 4: Antarctic ice velocity derived from ALOS PALSAR, Envisat ASAR, RADARSAT-2, and ERS-1/2 satellite radar interferometry, colour-coded on a logarithmic scale, and overlaid on a MODIS mosaic of Antarctica (Rignot et al, 2011).

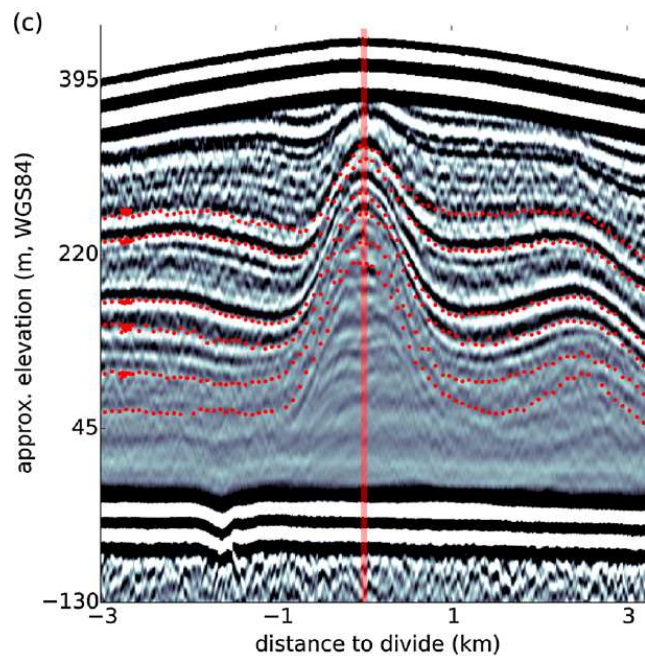


Figure 5: Radargram of isochrone stratigraphy across the Derwael ice rise (East Antarctica) (Drews et al, 2015).



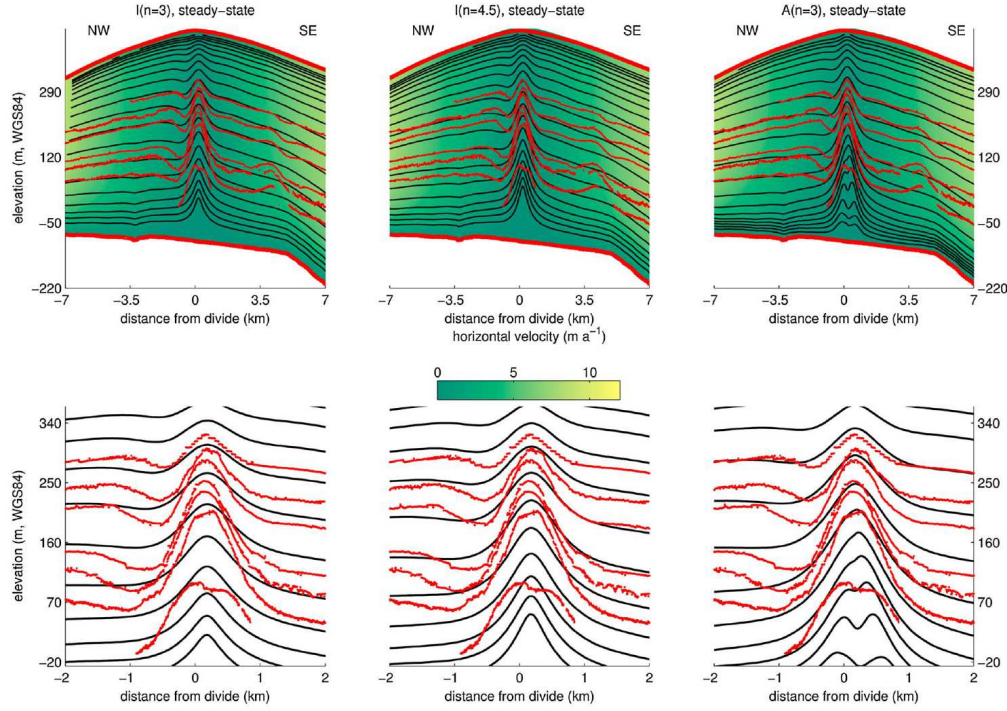


Figure 6: Simulated isochrones near the Derwael ice rise ice divide with a FS model (Elmer/ice) for different values of the flow exponent  $n$  in Glen’s flow law and isotropic (I) and anisotropic (A) ice (Drews et al, 2015).

While the effect operates at each ice divide, Raymond arches form when the divide has been stable over a long time. The characteristic time scale of formation is  $\tau_r = H/\dot{a}$ . For ice rises,  $\tau_r$  is typically 1000 years. However, in the interior of the Antarctic ice sheet  $\tau_r \approx 30\,000$  years, which makes them less visible in radargrams. For small-scale studies near ice divides, a FS or LMLa model needs to be employed (albeit that FS generally reproduces the Raymond effect better). Anisotropy is also a determining factor (Martín et al, 2009) (Fig. 6).

SIA models are also less useful when large topographic variability is observed (such as subglacial mountains and bedrock bumps). With a better and more detailed knowledge of subglacial topography of Greenland and Antarctic ice sheets, the view of a relatively flat bed underneath ice sheets has become seriously challenged. The ISMIP-HOM experiments (Ice Sheet Model Intercomparison on Higher-Order ice sheet Models; Pattyn et al (2008)) illustrate this perfectly. The purpose of this study was to gauge the difference between FS models and other models that incorporated membrane stresses (LMLa, L1L1, L1L2, ...).

The basic experiment considers a parallel-sided slab of ice with a mean ice thickness  $h = 1000$  m lying on a sloping bed with a mean slope  $\alpha = 0.5^\circ$ . This slope is maximum in  $x$  and zero in  $y$ . The basal topography is then defined as a series of sinusoidal oscillations with an amplitude of 500 m. The ice surface was taken flat and parallel to the general bedrock slope. The ice thickness has a mean value of 1000 m and is thinner above the bumps and thicker across the troughs. The surface elevation is defined as,

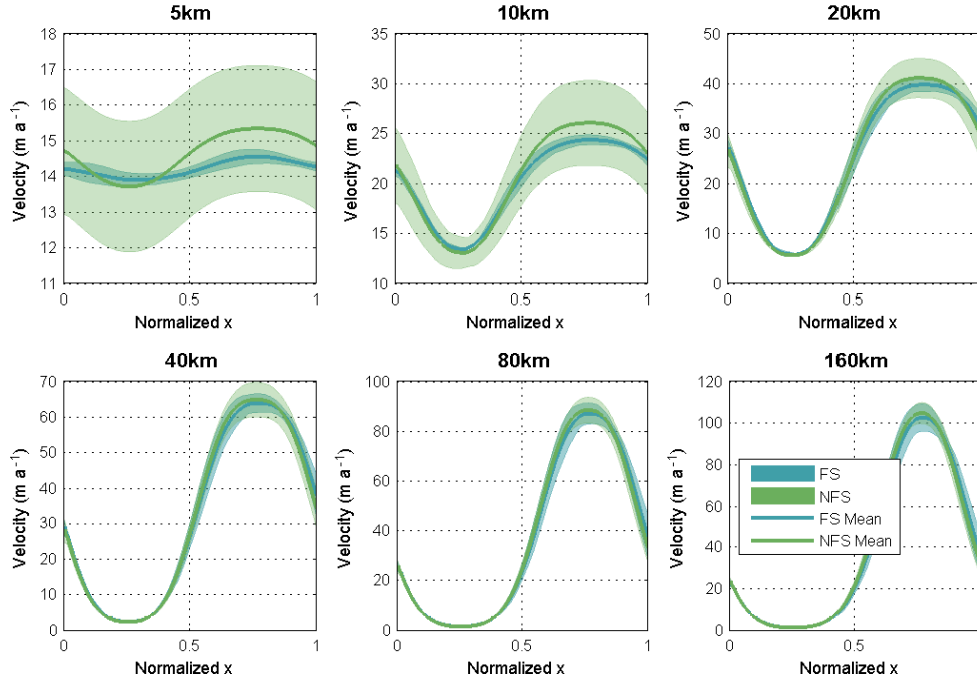


Figure 7: Results of the ISMIP-HOM bumpy bed experiment for different aspect ratios, i.e., different values for the length scale  $L$  for full Stokes (FS) and non-full Stokes (NFS) models (Pattyn et al, 2008).

$$s(x, y) = -x \cdot \tan \alpha . \quad (2.75)$$

The basal topography is then given by

$$b(x, y) = s(x, y) - 1000 + 500 \sin(\omega x) \cdot \sin(\omega y) , \quad (2.76)$$

where  $x \in [0, L]$  and  $L = 160, 80, 40, 20, 10$  and  $5$  km, respectively. The basal bumps have a frequency of  $\omega = 2\pi/L$ . This means that for each value of  $L$  the aspect ratio  $h/L$  increases with decreasing  $L$ . The numerical results are displayed in Fig 7. A distinction is made between full-Stokes (FS) and non-full-Stokes (NFS) models, such as LMLa, LTSML, L1L2 and L1L1. All parameters refer to horizontal surface velocities, which are determined as the norm of the horizontal components of the velocity field, defined by  $||\mathbf{v}_s|| = \sqrt{v_x^2 + v_y^2}$ . Velocities are displayed along a section  $y = L/4$ . The graphs show the mean velocity and its standard deviation along each section for both FS and NFS models. A distinct feature is that for both FS and NFS models (with exception of SIA) the amplitude in horizontal surface velocity decreases with increasing aspect ratio. For  $L=160$  km, the results are quite in agreement with the SIA solution (as the aspect ratio is also the smallest in this experiment). Remarkably, the SIA solution is the same for each experiment, as the local geometry, i.e. ice thickness and surface slope, is not changing; only the aspect ratio of the bumps does.

### 3 Numerical modelling of ice sheets and glaciers (SIA)

#### 3.1 Numerical methods

##### 3.1.1 FTCS scheme

In this section we will see how to solve numerically the equations that we have derived in the previous section. For this purpose we will choose a numerical method to do so. The most simple approach is to use the finite difference method. It consists of dividing up the model domain in regularly-spaced nodes on which the variables will be calculated. In order to derive spatial and temporal gradients, the method is based on replacing derivatives by discrete spatial/temporal differences or gradients, based on Taylor series,

$$H(t + \Delta t) \approx H(t) + \Delta t \frac{\partial H}{\partial t} + \frac{(\Delta t)^2}{2} \frac{\partial^2 H}{\partial t^2} + \frac{(\Delta t)^3}{6} \frac{\partial^3 H}{\partial t^3} + \dots \quad (3.1)$$

Normally, terms higher than the first derivative are neglected, so that the time derivative is approximated by

$$\frac{\partial H}{\partial t} \approx \frac{H_{t+\Delta t} - H_t}{\Delta t} \quad (3.2)$$

Since time can be considered a regularly spaced vector with spacing of  $\Delta t$ , it is easier to use the following notation,

$$\frac{\partial H}{\partial t} \approx \frac{H_{t+1} - H_t}{\Delta t} \quad (3.3)$$

A similar approach is used for spatial derivatives, but contrary to the time derivative centred in space,

$$\frac{\partial H}{\partial x} \approx \frac{H_{i+1} - H_{i-1}}{2\Delta x} \quad (3.4)$$

$$\frac{\partial^2 H}{\partial x^2} \approx \frac{H_{i+1} - 2H_i + H_{i-1}}{(\Delta x)^2} \quad (3.5)$$

Such scheme is called FTCS or Forward in Time, Central in Space and illustrated in Fig. 8. The second derivative is determined by calculating local spatial gradients between consecutive grid points and taking the gradient across these points. The result is a symmetric derivative around  $i$ , involving only the immediate neighbouring grid points  $i + 1$  and  $i - 1$  (Fig. 8).

##### 3.1.2 Numerical solution to a diffusive equation

In order to demonstrate the use of finite differences, we will consider the example of the evolution of a hillslope made from weathered material. For the sake of simplicity we consider a symmetric rectilinear slope in one dimension with a watershed or drainage divide in the centre. The material is transported down both slopes due to steady creep, i.e., a slow mass movement. This implies that the mass moves in a diffusive way, i.e. a transfer of material from point to point along the slope. The process can be mathematically expressed as a diffusion equation for the thickness of the weathered material,

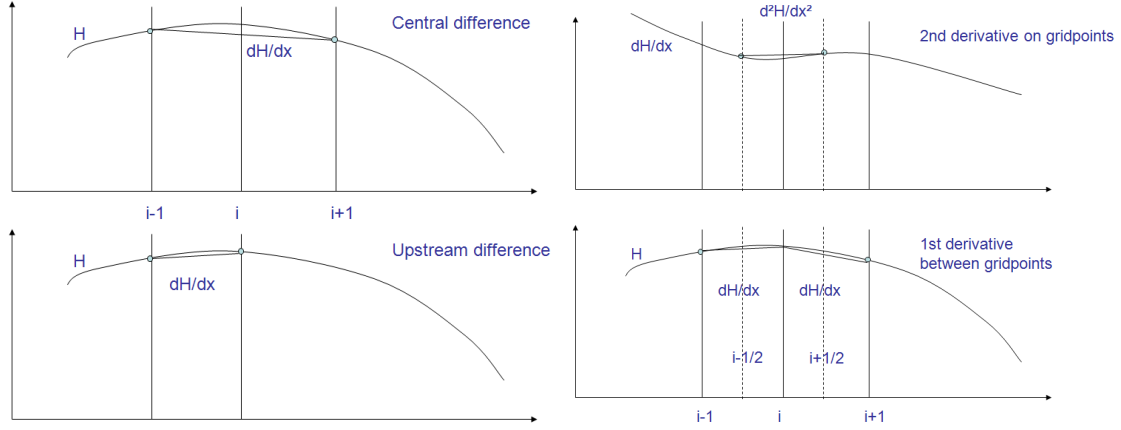


Figure 8: Spatial derivatives according to backward (upstream) and central differences for first (left) and second (right) order derivatives.

$$\frac{\partial H}{\partial t} = D \frac{\partial^2 H}{\partial x^2} \quad (3.6)$$

where  $D$  is a diffusion coefficient. Using finite differences, the thickness of the weathered material along the flow line on the next time step is written as:

$$H_{i,t+1} = H_{i,t} + \frac{D\Delta t}{(\Delta x)^2} (H_{i+1,t} - 2H_{i,t} + H_{i-1,t}) \quad (3.7)$$

To solve this equation, we need to define the numerical grid, its initial state and the boundary conditions. Consider a horizontal domain of  $n = 101$  evenly spaced grid points that represents the horizontal scale from  $-1$  to  $+1$  (the watershed will be at  $x = 0$ ), and an initial linear hillslope  $H$  culminating at  $x = 0$  and hence defined by

$$H_{i,t=0} = 1 - |x_i| \quad (3.8)$$

During the slope evolution, mass will be transferred from the higher parts of the hillslope to the lower parts (edges of the domain). Here we consider that all material arriving at the edge of the domain is automatically removed. This corresponds to keeping the elevation of the edge grid points constant in time ( $H_1 = H_n = 0$ ). Such a boundary condition is called a Dirichlet boundary condition. We then let the hillslope evolve in time through an iterative process by calculating on each time step  $t+1$  a new elevation  $H_{i,t+1}$  according to (3.7). At the end of each iteration this solution is copied back to the initial value of  $H_{i,t}$ . This allows us to only keep two arrays  $H_t$  and  $H_{i,t+1}$  in memory. (3.7) is also computed in an iterative fashion by calculating  $H_{i,t+1}$  for each grid point  $2 < i < n-1$ . In the Matlab code example below, the diffusion coefficient  $D$  was replaced by  $D\Delta t$ ,

```
n=101;
D=2e-4;
x=linspace(-1,1,n);
H=1-abs(x);
dx=2/(n-1);
```

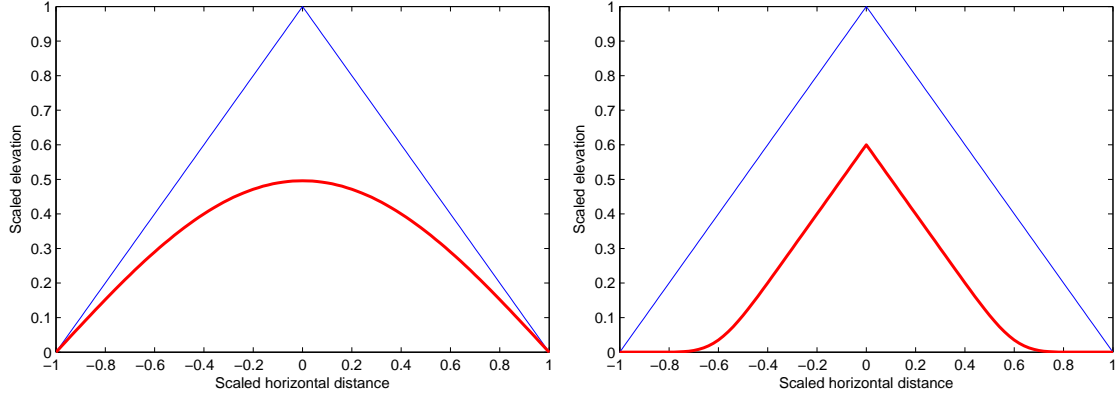


Figure 9: Initial (blue) and final (red) profiles of the hillslope due to diffusive mass transport according to (3.7) (left) and due to advection according to (3.10) (right).

```

Hn=H;
H0=H;
for t=1:1000
    for i=2:n-1
        Hn(i)=H(i)+D*(H(i+1)-2*H(i)+H(i-1))/dx^2;
    end
    H=Hn;
end

```

The artificial initial linear slope becomes gradually transformed into the convex profile that characterizes plastic-viscous flow (including creep) of non-cohesive material. Viscous-plastic flow can be considered as a point-to-point transfer of waste: each point on the slope receives, per unit time, a quantity of waste (expressed on the profile in terms of thickness  $H$ ) from the next higher point, and loses another quantity of waste to the next lower point (Fig 9).

### 3.1.3 Numerical solution to an advection equation

Advection is a process in which material is transported rapidly with the motion of a fluid (or the gravity-driven motion of the material itself). In our example this corresponds to the displacement of weathered material in suspension within a thin water layer with a constant speed  $u$ . The magnitude of the transport will be a function of the surface gradient of the hillslope,

$$\frac{\partial H}{\partial t} = u \frac{\partial H}{\partial x} \quad (3.9)$$

Numerically, this is written as, ad

$$H_{i,t+1} = H_{i,t} + \frac{u\Delta t}{(2\Delta x)} (H_{i+1,t} - H_{i-1,t}) \quad (3.10)$$

A major difference with the diffusion process is that transport due to advection is a function of the sign of the slope, hence the velocity of the fluid is negative for positive surface slopes, and positive for negative slopes. A further complication is that advection

processes are inherently unstable. To overcome this, one can use upstream differences instead of central differences and/or include a small amount of artificial diffusion in order to stabilize the numerical integration. The Matlab code therefore becomes,

```
n=101;
u=4e-4;
D=4e-6;
x=linspace(-1,1,n);
H=1-abs(x);
dx=2/(n-1);
Hn=H;b
H0=H;
for t=1:1000
    for i=2:n-1
        if x(i)>=0
            Hn(i)=H(i)+u*(H(i+1)-H(i-1))/(2*dx) ...
                +D*(H(i+1)-2*H(i)+H(i-1))/dx^2;
        else
            Hn(i)=H(i)-u*(H(i+1)-H(i-1))/(2*dx) ...
                +D*(H(i+1)-2*H(i)+H(i-1))/dx^2;
        end
    end
end
```

Applied to the rectilinear slope taken from the previous example, run-off results in a concave evolution of the slope (Fig. 9). The slope now takes a concave form at the bottom of the slope, and a more or less rectilinear slope at the head of the profile. The advection process is – contrary to the diffusion process – a fast transport of material due to the velocity of the surrounding medium (in this case water that takes material in suspension), and not a point-by-point transfer along the slope of the material itself. The magnitude of the process is determined by the surface slope.

### 3.2 Explicit numerical solution for the ice-sheet equation

In order to solve the derived equations (2.74) and (2.59) numerically, we will employ the same numerical methods as illustrated above. In the most simple case, we consider a flowline across an ice sheet. Neglecting basal sliding, the vertical mean horizontal velocity is then written as

$$\bar{u} = -\frac{2A}{n+2} (\rho_i g)^n \left| \frac{\partial s}{\partial x} \right|^{n-1} \frac{\partial s}{\partial x} h^{n+1} \quad (3.11)$$

where  $s = b + h$  is the surface elevation of the ice sheet. Basal melting is neglected and surface mass balance is governed by a constant accumulation rate  $M_s = \dot{a}$ , so that (2.74) transforms to,

$$\frac{\partial h}{\partial t} = -\frac{\partial(\bar{u}h)}{\partial x} + \dot{a} = -\frac{\partial q}{\partial x} + \dot{a} \quad (3.12)$$

Numerically, this is written as,

$$h_{i,t+1} = h_{i,t} + \left[ q_{i+\frac{1}{2},t} - q_{i-\frac{1}{2},t} \right] \frac{\Delta t}{\Delta x} + \dot{a} \Delta t \quad (3.13)$$

where the fluxes inbetween grid points are defined as,

$$q_{i+\frac{1}{2},t} = \frac{2A}{n+2}(\rho_i g)^n \left( \frac{h_{i+1,t} + b_{i+1,t} - h_{i,t} - b_{i,t}}{\Delta x} \right)^n \left( \frac{h_{i,t} + h_{i+1,t}}{2} \right)^{n+2} \quad (3.14)$$

$$q_{i-\frac{1}{2},t} = \frac{2A}{n+2}(\rho_i g)^n \left( \frac{h_{i,t} + b_{i,t} - h_{i-1,t} - b_{i-1,t}}{\Delta x} \right)^n \left( \frac{h_{i,t} + h_{i-1,t}}{2} \right)^{n+2} \quad (3.15)$$

Since a pure advection equation can be numerically unstable in FTCS, solving it requires a closer look. In reality, the continuity equation is a diffusion equation and not a pure advection equation, due to the dependence of  $q$  on  $\partial h / \partial x$ , as shown hereunder.

$$\begin{aligned} \frac{\partial h}{\partial t} &= -\frac{\partial}{\partial x}(\bar{u}h) + \dot{a} \\ &= \frac{\partial}{\partial x} \left( d \frac{\partial(h+b)}{\partial x} \right) + \dot{a} \end{aligned} \quad (3.16)$$

where the (spatially-varying) diffusion coefficient  $d$  is defined by

$$\begin{aligned} d &= -\bar{u}h \left( \frac{\partial(h+b)}{\partial x} \right)^{-1} \\ &= -\frac{2A}{n+2}(\rho_i g)^n \left| \frac{\partial(h+b)}{\partial x} \right|^{n-2} \frac{\partial(h+b)}{\partial x} h^{n+2} \end{aligned} \quad (3.17)$$

Diffusion terms (or transformed flux terms) are evaluated between the grid points

$$d_{i+\frac{1}{2},t} = \frac{2A}{n+2}(\rho_i g)^n \left| \frac{h_{i+1,t} + b_{i+1,t} - h_{i,t} - b_{i,t}}{\Delta x} \right|^{n-1} \left( \frac{h_{i,t} + h_{i+1,t}}{2} \right)^{n+2} \quad (3.18)$$

$$\begin{aligned} h_{i,t+1} &= h_{i,t} + \frac{\Delta t}{(\Delta x)^2} \left[ d_{i+\frac{1}{2},t} (h_{i+1,t} + b_{i+1,t} - h_{i,t} - b_{i,t}) - \right. \\ &\quad \left. d_{i-\frac{1}{2},t} (h_{i,t} + b_{i,t} - h_{i-1,t} - b_{i-1,t}) \right] + \dot{a} \Delta t \end{aligned} \quad (3.19)$$

The diffusive grid is called a staggered grid, similar to the flux-equation shown before. Boundary conditions for (3.19) are zero ice thickness at the boundaries. Since  $d$  is calculated on the staggered grid, boundary conditions do not need to be defined. Below is a Matlab code for the explicit solution of an ice sheet along a flow-line. The result is shown in Fig 10.

```
m=51;
L=1.5e6; % length of domain (m)
h=zeros(m,1);
time_end=20000.;
dt=2.; % time step (years)
dx=L/(m-1); % grid spacing (m)
```

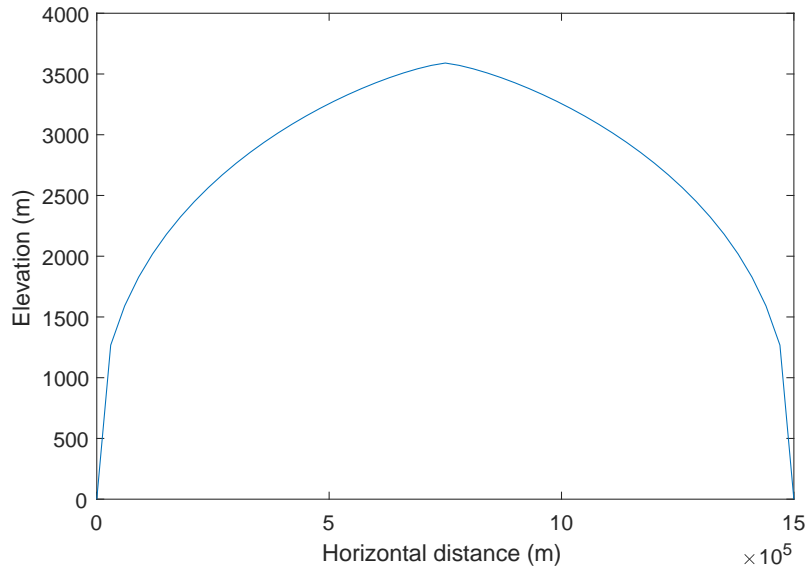


Figure 10: Evolution of an ice sheet on a flat bedrock based on the solution of (3.19).

```
x=linspace(0,L,m)'; % horizontal distance
b=zeros(m,1); % bedrock elevation
d=zeros(m,1);

% Physical constants
A=1e-16; % Ice flow parameter
rho=910.; % Ice density
grav=9.81; % Gravitation constant
n=3; % Glen index
a=0.3; % Surface mass balance

% time stepping
time_lapse = round(time_end/dt)+1;
h2=h;
for i=1:time_lapse
    slope=diff(b+h)/dx; % slope on staggered grid
    for j=1:m-1
        hstag=(h(j+1)+h(j))/2.; % ice thickness on staggered grid
        d(j)=2./(n+2.)*A*hstag^2*slope(j)^2*(rho*...
            grav*hstag)^n;
    end
    for j=2:m-1
        h2(j)=h(j)+(d(j)*slope(j)-d(j-1)*slope(j-1))*dt/dx+a*dt;
    end
    h=h2;
end %% end of time stepping
```

### 3.3 Semi-implicit numerical solution of the ice-sheet equation

Despite the stability of FTCS written as a diffusive equation, solving (3.19) still requires very small time steps. Greater numerical stability can be obtained by writing (3.19) as an implicit equation by evaluating its right-hand side on timestep  $t+1$  instead of  $t$ . However,



since diffusion coefficients  $d$  are still a function of  $h$ , this will be an semi-implicit method, which remains inferior in stability compared to the full implicit method. In this case, (3.19) is rewritten as:

$$h_{i,t+1} = h_{i,t} + \frac{\Delta t}{(\Delta x)^2} \left[ d_{i+\frac{1}{2},t} (h_{i+1,t+1} + b_{i+1,t} - h_{i,t+1} - b_{i,t}) - d_{i-\frac{1}{2},t} (h_{i,t+1} + b_{i,t} - h_{i-1,t+1} - b_{i-1,t}) \right] + \dot{a}\Delta t \quad (3.20)$$

$$\begin{aligned} h_{i,t+1} - \frac{\Delta t}{(\Delta x)^2} \left[ d_{i+\frac{1}{2},t} (h_{i+1,t+1} - h_{i,t+1}) - d_{i-\frac{1}{2},t} (h_{i,t+1} - h_{i-1,t+1}) \right] \\ = \frac{\Delta t}{(\Delta x)^2} \left[ d_{i+\frac{1}{2},t} (b_{i+1,t} - b_{i,t}) - d_{i-\frac{1}{2},t} (b_{i,t} - b_{i-1,t}) \right] + \dot{a}\Delta t \end{aligned} \quad (3.21)$$

Therefore, we can define the following coefficients that are a function of  $h$  and will need to be updated every time step in the numerical integration:

$$\begin{aligned} \alpha_i &= \frac{\Delta t}{(\Delta x)^2} d_{i-\frac{1}{2},t} & \beta_i &= 1 + \frac{\Delta t}{(\Delta x)^2} (d_{i-\frac{1}{2},t} + d_{i+\frac{1}{2},t}) \\ \gamma_i &= \frac{\Delta t}{(\Delta x)^2} d_{i+\frac{1}{2},t} & \delta_i &= \alpha_i b_{i-1,t} - (\beta_i - 1)b_{i,t} + \gamma_i b_{i+1,t} + h_{i,t} + \dot{a}\Delta t \end{aligned}$$

so that,

$$-\alpha_i h_{i-1,t+1} + \beta_i h_{i,t+1} - \gamma_i h_{i+1,t+1} = \delta_i \quad (3.22)$$

This system of equations can be written in matrix notation as follows.

$$\begin{bmatrix} \beta_1 & -\gamma_1 & 0 & 0 & \cdots & 0 & 0 & 0 \\ -\alpha_2 & \beta_2 & -\gamma_2 & 0 & \cdots & 0 & 0 & 0 \\ 0 & -\alpha_3 & \beta_3 & -\gamma_3 & \cdots & 0 & 0 & 0 \\ \vdots & \vdots & \vdots & \vdots & \ddots & \vdots & \vdots & \vdots \\ 0 & 0 & 0 & 0 & \cdots & -\alpha_{m-1} & \beta_{m-1} & -\gamma_{m-1} \\ 0 & 0 & 0 & 0 & \cdots & 0 & -\alpha_m & \beta_m \end{bmatrix} \begin{bmatrix} h_1 \\ h_2 \\ h_3 \\ \vdots \\ h_{m-1} \\ h_m \end{bmatrix} = \begin{bmatrix} \delta_1 \\ \delta_2 \\ \delta_3 \\ \vdots \\ \delta_{m-1} \\ \delta_m \end{bmatrix} \quad (3.23)$$

This is a tridiagonal system of equations, meaning that non-zero elements occur on the diagonal axis as well as the two adjacent axes. All other elements of the matrix are zero. Such a system can be easily solved with the method below. Consider now the following two equations that hold between two adjacent grid points:

$$h_i = f_i h_{i+1} + g_i \quad (3.24)$$

$$h_{i-1} = f_{i-1} h_i + g_{i-1} \quad (3.25)$$

By definition we can derive from (3.22) and (3.25) that

$$\begin{aligned} \alpha_i h_{i-1} &= \alpha_i f_{i-1} h_i + \alpha_i g_{i-1} \\ &= \beta_i h_i - \gamma_i h_{i+1} - \delta_i \end{aligned}$$

Combining both equations then results in

$$h_i = \frac{\gamma_i}{\beta_i - \alpha_i f_{i-1}} h_{i-1} + \frac{\delta_i + \alpha_i g_{i-1}}{\beta_i - \alpha_i f_{i-1}} \quad (3.26)$$

where,

$$f_i = \frac{\gamma_i}{\beta_i - \alpha_i f_{i-1}}, \quad g_i = \frac{\delta_i + \alpha_i g_{i-1}}{\beta_i - \alpha_i f_{i-1}}$$

For both the explicit and implicit solution, boundary conditions need to be defined, i.e., ice thickness at the first and last grid point, as well as conditions pertaining to the ice sheet velocity. For simplicity, we will consider that ice thickness at the lateral boundaries is zero (edge of the ice sheet), or  $h_1 = h_m = 0$ . We can therefore derive the boundary conditions for both  $f_1$  and  $g_1$  (or for  $f_m$  and  $g_m$ ). For the first grid point, we have according to (3.24) that  $f_1 = g_1 = 0$ , from which all remainder values of  $f_i$  and  $g_i$  can be calculated. Ice thickness on  $t + 1$  is then calculated starting from the last grid point with the condition that  $h_m = 0$ :

$$\begin{aligned} h_{m-1} &= f_{m-1} h_m + g_{m-1} \\ h_{m-2} &= f_{m-2} h_{m-1} + g_{m-2} \\ &\vdots \\ h_1 &= f_1 h_2 + g_1 \end{aligned}$$

The solution is called solving a “tridiagonal system” of equations. An example of an implicit time-stepping scheme for the same flowline ice-sheet model is illustrated below and the resulting ice-sheet profile is shown in Fig. 11.

```
m=51;
L=1.5e6; % length of domain (m)
h=zeros(m,1);
time_end=20000.;
dt=10.; % time step (years)
dx=L/(m-1); % grid spacing (m)
x=linspace(0,L,m)'; % horizontal distance
b=zeros(m,1); % bedrock elevation
d=zeros(m,1);
alph=zeros(m,1);
bet=zeros(m,1);
gamm=zeros(m,1);
delta=zeros(m,1);
f=zeros(m,1);
g=zeros(m,1);

% Physical constants
A=1e-16; % Ice flow parameter
rho=910.; % Ice density
grav=9.81; % Gravitation constant
n=3; % Glen index
a=0.3; % Surface mass balance
```

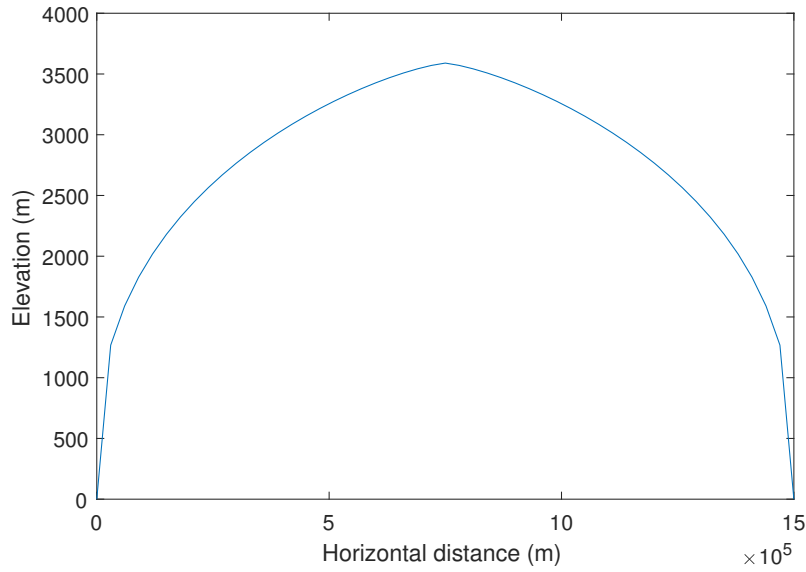


Figure 11: Evolution of an ice sheet on a flat bedrock based on the solution of (3.21). Time steps can be significantly increased, which enables faster calculation time with a semi-implicit method.

```
% time stepping
time_lapse = round(time_end/dt)+1;
dtdx=dt/dx^2;
for i=1:time_lapse
    slope=diff(b+h)/dx; % slope on staggered grid
    for j=1:m-1
        hstag=(h(j+1)+h(j))/2.; % ice thickness on staggered grid
        d(j)=2./(n+2.)*A*hstag^2*slope(j)^2*(rho*grav*hstag)^n;
    end
    for j=2:m-1
        gamm(j)=d(j)*dtdx;
        alph(j)=d(j-1)*dtdx;
        bet(j)=1.+gamm(j)+alph(j);
        delta(j)=h(j)+a*dt+alph(j)*b(j-1)-(bet(j)-1)*b(j) ...
            +gamm(j)*b(j+1);
    end
    for j=2:m-1
        f(j)=gamm(j)/(bet(j)-alph(j)*f(j-1));
        g(j)=(delta(j)+alph(j)*g(j-1))/(bet(j)-alph(j)*f(j-1));
    end
    h2=zeros(m,1);
    for j=m-1:-1:1
        h2(j)=g(j)+f(j)*h2(j+1);
    end
    h=h2;
end %% end of time stepping
```

### 3.4 Verification of SIA solutions

#### 3.4.1 The Nye-Vialov analytical solution

This analytical solution is valid for an ice sheet resting on a flat bed ( $b = 0$ ) and for a constant accumulation rate  $\dot{a}$ . In a steady state, it follows from mass continuity that

$$\dot{a}x = uh = -A_0 \left| \frac{\partial h}{\partial x} \right|^{n-1} \frac{\partial h}{\partial x} \quad (3.27)$$

where

$$A_0 = \frac{2A}{n+2} (\rho_i g)^n \quad (3.28)$$

Integrating (3.27) leads to

$$\left( h^{1+2/n} \frac{\partial h}{\partial x} \right)^n = -\frac{\dot{a}}{A_0} x \quad (3.29)$$

$$\frac{\partial}{\partial x} (h^{2+2/n}) = -\frac{2n+2}{n} \left( \frac{\dot{a}}{A_0} \right)^{1/n} x^{1/n} \quad (3.30)$$

$$h^{2+2/n} = h_0^{2+2/n} \left( 1 - \left( \frac{|x-L|}{L} \right)^{1+1/n} \right) \quad (3.31)$$

where

$$h_0^{2+2/n} = \frac{2n+2}{n+1} \left( \frac{\dot{a}}{A_0} \right)^{1/n} L^{1+1/n} \quad (3.32)$$

A comparison between the semi-implicit steady-state solution and the analytical Nye-Vialov solution is shown in Fig. 12. We can also test the mass conservation of the numerical method. From a steady state ice sheet it follows that (for  $\dot{a} = \text{constant}$ ):

$$\frac{\partial(\bar{u}h)}{\partial x} = \dot{a} \quad \text{or (by integration)} \quad \bar{u}_x h_x = \int_0^x \dot{a} dx = \dot{a}x \quad (3.33)$$

This is illustrated in Fig. 13.

### 3.5 Two-dimensional ice-sheet model

In this section, adapted from MacAyeal (1997), we shall construct a two-dimensional ice-sheet model using the finite-difference method. We will employ sparse matrix algebra that offers significant computational efficiencies compared to traditional ADI (alternating-direct-implicit) methods, as illustrated in Section 3.5.2.

For simplicity, we will first derive a non-dimensional expression of the ice sheet equation derived above. For Glen's flow law with exponent  $n = 3$ , and a flat bedrock, so that  $s = h$ , the ice flux  $q$  for the ice sheet can be written as:

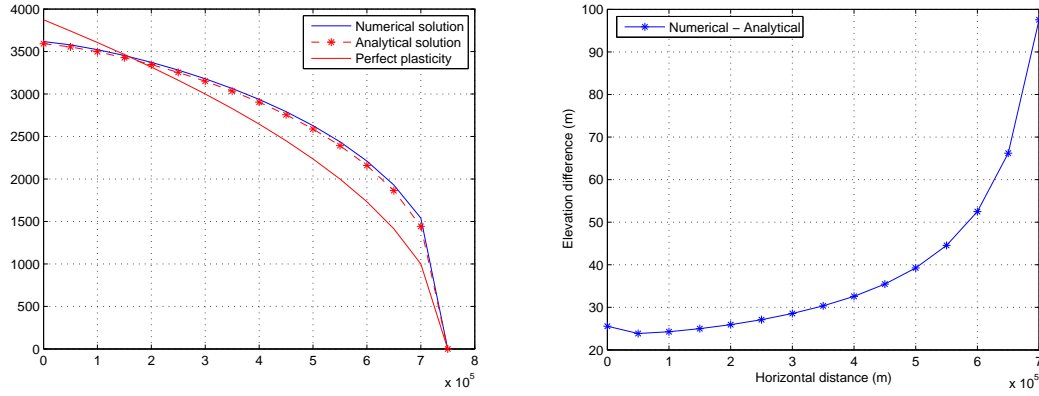


Figure 12: Difference between steady-state modeled (blue) and analytical (red) ice sheet profiles; differences increase towards the edge of the ice sheet domain, where ice fluxes are the highest

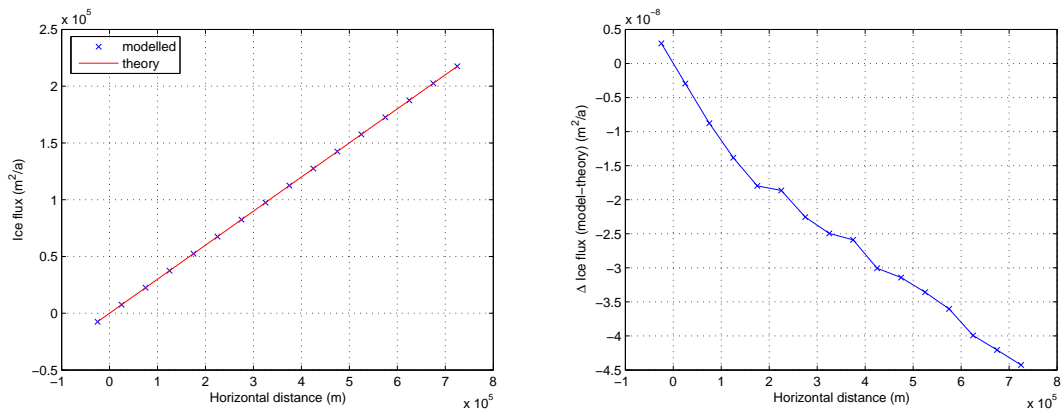


Figure 13: Plot of steady state ice flux versus iterated accumulation rate along the flow-line (left); difference between both (right).

$$\frac{\partial h}{\partial t} = \dot{a} - \nabla \mathbf{q} \quad (3.34)$$

$$\mathbf{q} = \frac{-2(\rho g)^3 A h^5}{5} (\nabla h \cdot \nabla h) \nabla h \quad (3.35)$$

A quick check of the units reveals that  $\mathbf{q}$  has dimension of  $\text{m}^2 \text{s}^{-1}$ , it is thus interpreted as a volume flux per unit cross-width. With substitution of the expression given in (3.35) for  $\mathbf{q}$  in (3.34), the mass balance equation becomes

$$\frac{\partial h}{\partial t} = \dot{a} - \nabla \cdot \left( \frac{2(\rho g)^3 A h^5}{5} (\nabla h)^3 \right) \quad (3.36)$$

It will be convenient for what follows to adopt nondimensional variables. Accordingly, we set

$$\begin{aligned} h &\rightarrow Zs \\ x, y &\rightarrow Lx, Ly \end{aligned}$$

and choose scales  $Z$  and  $L$  to satisfy the following identity

$$\frac{2A(\rho g)^3 Z^8}{5L^4} = \dot{a} \quad (3.37)$$

For  $L = 750 \text{ km}$  and  $\dot{a} = 0.3 \text{ m a}^{-1}$ , the above expression gives  $Z = 2756.7 \text{ m}$ . Thus a non-dimensional surface elevation  $s$  of 1 corresponds with a dimensional surface elevation of 2756.7m. Our adoption of non-dimensional variables means nothing more than an agreement about what “meter stick” we plan to measure space and velocity with. The use of non-dimensional variables is completely arbitrary. We choose to use non-dimensional variables because of the possible simplifications and clarifications to the equations which may come later. In non-dimensional form, the governing equation becomes

$$\frac{\partial s}{\partial t} = 1 + \nabla \cdot ((\nabla s)^3 s^5) \quad (3.38)$$

For convenience, we define an effective diffusivity  $d = (\nabla s \cdot \nabla s) s^5$  to render the above equation into a form that is easily linearised:

$$\frac{\partial s}{\partial t} = 1 + \nabla \cdot (d \nabla s) \quad (3.39)$$

### 3.5.1 Implicit time-stepping with a staggered grid

Following finite-difference conventions, we adopt a staggered finite-difference scheme where variables  $s$  and  $d$  are defined as shown in Fig. 14. The discrete form of (3.39) is composed of the following parts

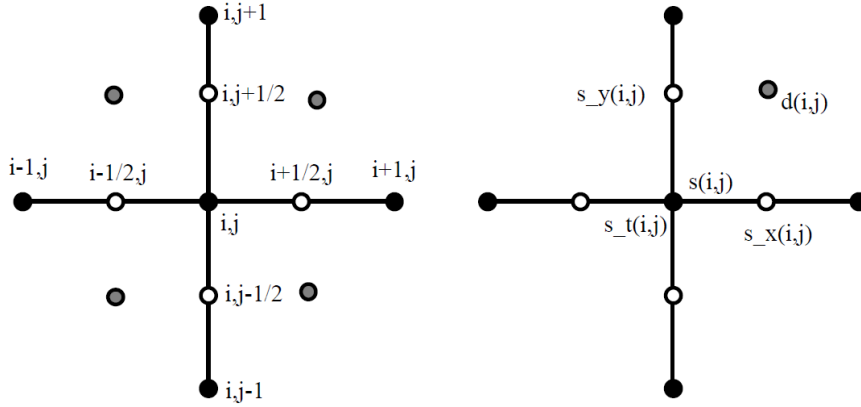


Figure 14: Staggered grid used for solving the ice sheet equation in a two-dimensional model.

$$\begin{aligned}
 d_{i,j}^\ell &= \left[ \frac{1}{4} (s_{i,j}^\ell + s_{i+1,j}^\ell + s_{i+1,j+1}^\ell + s_{i,j+1}^\ell) \right]^5 \\
 &\times \frac{1}{4\Delta^2} \left[ (s_{i+1,j}^\ell - s_{i,j}^\ell + s_{i+1,j+1}^\ell - s_{i,j+1}^\ell)^2 \right. \\
 &\left. + (s_{i,j+1}^\ell - s_{i,j}^\ell + s_{i+1,j+1}^\ell - s_{i+1,j}^\ell)^2 \right]
 \end{aligned} \tag{3.40}$$

$$\begin{aligned}
 \frac{\partial}{\partial x} \left( d \frac{\partial s}{\partial x} \right) \Big|_{i,j} &= \frac{1}{2\Delta^2} \left[ (d_{i,j}^\ell + d_{i,j-1}^\ell) (s_{i+1,j}^{\ell+1} + s_{i,j}^{\ell+1}) \right. \\
 &\quad \left. - (d_{i-1,j}^\ell + d_{i-1,j-1}^\ell) (s_{i,j}^{\ell+1} + s_{i-1,j}^{\ell+1}) \right]
 \end{aligned} \tag{3.41}$$

$$\begin{aligned}
 \frac{\partial}{\partial y} \left( d \frac{\partial s}{\partial y} \right) \Big|_{i,j} &= \frac{1}{2\Delta^2} \left[ (d_{i,j}^\ell + d_{i-1,j}^\ell) (s_{i,j+1}^{\ell+1} + s_{i,j}^{\ell+1}) \right. \\
 &\quad \left. - (d_{i,j-1}^\ell + d_{i-1,j-1}^\ell) (s_{i,j}^{\ell+1} + s_{i,j-1}^{\ell+1}) \right]
 \end{aligned} \tag{3.42}$$

where  $\Delta$  is the grid spacing (assumed to be the same in the two spatial directions), subscripts denote the grid point where the designated variables are evaluated, and the superscripts  $\ell$  and  $\ell + 1$  denote the time-step level at which the designated variables are evaluated. Convention dictates that variables at time step  $\ell$  are considered known (possibly from the specification of an initial condition) and variables at time step  $\ell + 1$  are unknown. The goal of the finite-difference model is to determine the variables at time step  $\ell + 1$  in an iterative fashion so to accomplish a time marching.

The above finite-difference parts are put together to yield the following finite-difference equation for the  $s_{i,j}^{\ell+1}$  (implicit time step):

$$\begin{aligned}
 s_{i,j}^{\ell+1} & \left[ \frac{1}{\Delta t} + \frac{1}{\Delta^2} (d_{i,j}^\ell + d_{i-1,j}^\ell + d_{i,j-1}^\ell + d_{i-1,j-1}^\ell) \right] \\
 & + s_{i,j+1}^{\ell+1} \left[ \frac{-1}{2\Delta^2} (d_{i,j}^\ell + d_{i-1,j}^\ell) \right] \\
 & + s_{i,j-1}^{\ell+1} \left[ \frac{-1}{2\Delta^2} (d_{i,j-1}^\ell + d_{i-1,j-1}^\ell) \right] \\
 & + s_{i+1,j}^{\ell+1} \left[ \frac{-1}{2\Delta^2} (d_{i,j}^\ell + d_{i,j-1}^\ell) \right] \\
 & + s_{i-1,j}^{\ell+1} \left[ \frac{-1}{2\Delta^2} (d_{i-1,j}^\ell + d_{i-1,j-1}^\ell) \right] = 1 + \frac{s_{i,j}^\ell}{\Delta t} \quad (3.43)
 \end{aligned}$$

The above equation may be conveniently expressed in matrix notation as follows:

$$\mathbf{A} s^{\ell+1} = \mathbf{R} \quad (3.44)$$

where  $s^\ell$  is the column vector composed of the values of  $s_{i,j}^\ell$  arranged by the order in which the grid points are numbered. Thus, if grid point  $(i, j)$  is numbered  $\gamma_{i,j}$  where  $\gamma_{i,j}$  is an integer in the interval  $[1, 31^2]$ , the  $p$ 'th element of  $s^\ell$  is the value of  $s^\ell$  at the grid point  $(i, j)$  whose  $\gamma_{i,j}$  is equal to  $p$ . The matrix element  $A_{pq}$  describes how the solution at grid point  $\gamma_{i,j} = p$  depends on the solution at grid point  $\gamma_{i,j} = q$ . The matrix-construction algorithm may be summarized from the finite-difference version of the problem described above as follows:

$$\begin{aligned}
 s_{i,j}^{\ell+1} & \left[ \frac{1}{\Delta t} + \frac{1}{\Delta^2} (d_{i,j}^\ell + d_{i-1,j}^\ell + d_{i,j-1}^\ell + d_{i-1,j-1}^\ell) \right] \rightarrow A_{\gamma_{i,j}, \gamma_{i,j}} \\
 s_{i,j+1}^{\ell+1} & \left[ \frac{-1}{2\Delta^2} (d_{i,j}^\ell + d_{i-1,j}^\ell) \right] \rightarrow A_{\gamma_{i,j}, \gamma_{i,j+1}} \\
 s_{i,j-1}^{\ell+1} & \left[ \frac{-1}{2\Delta^2} (d_{i,j-1}^\ell + d_{i-1,j-1}^\ell) \right] \rightarrow A_{\gamma_{i,j}, \gamma_{i,j-1}} \\
 s_{i+1,j}^{\ell+1} & \left[ \frac{-1}{2\Delta^2} (d_{i,j}^\ell + d_{i,j-1}^\ell) \right] \rightarrow A_{\gamma_{i,j}, \gamma_{i+1,j}} \\
 s_{i-1,j}^{\ell+1} & \left[ \frac{-1}{2\Delta^2} (d_{i-1,j}^\ell + d_{i-1,j-1}^\ell) \right] \rightarrow A_{\gamma_{i,j}, \gamma_{i-1,j}} \\
 1 + \frac{s_{i,j}^\ell}{\Delta t} & \rightarrow R_{\gamma_{i,j}} \quad (3.45)
 \end{aligned}$$

These “matrix-stuffing” conventions apply for grid points that are not on the boundaries of the numerical domain. For the boundaries of the simple ice-sheet model, we apply the simple condition:

$$A_{\gamma_{i,j}, \gamma_{i,j}} = 1 \quad \text{for } i = 1, i_{\max} \text{ or } j = 1, j_{\max} \quad (3.46)$$

with all other elements in rows of  $\mathbf{A}$  corresponding to these boundary grid points being zero. We also have, for the boundary nodes

$$R_{\gamma_{i,j}} = 0 \quad \text{for } i = 1, i_{\max} \text{ or } j = 1, j_{\max} \quad (3.47)$$



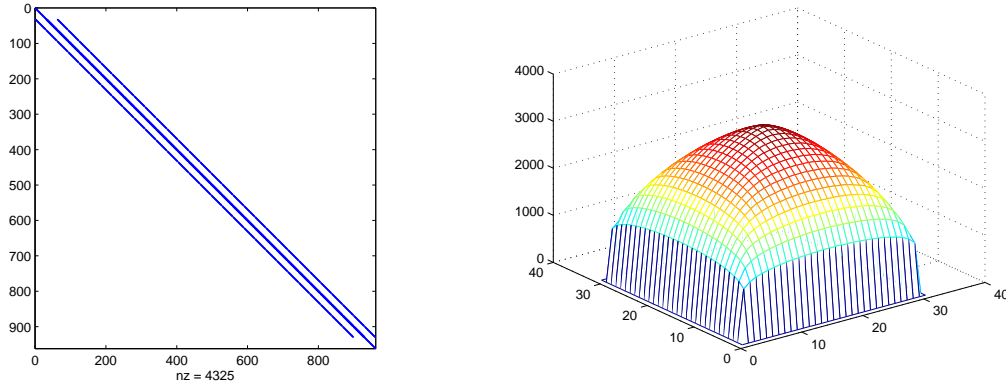


Figure 15: Left: Non-zero elements in the sparse matrix  $\mathbf{A}$ . Right: Two-dimensional ice sheet solved using the sparse matrix solver illustrated above.

The time stepping model ice-sheet model is thus described by solution of the linear equation  $\mathbf{A}s^{\ell+1} = \mathbf{R}$  for as many time steps as desired starting from a specified initial condition  $s^0$ . After the solution of the linear equation at each time step, the matrix  $\mathbf{A}$  and the right-hand-side vector  $\mathbf{R}$  must be reconstructed using updated values of the  $d_{i,j}^\ell$ 's and the  $s_{i,j}^{\ell+1}$ 's.

### 3.5.2 A digression about sparse matrices

Before using the above-described finite-difference model, we must consider the fact that the matrix  $\mathbf{A}$  can be very large, and may stress the limits of computer memory just for its storage. For the simple ice sheet on a flat bed, the  $31 \times 31$  finite-difference grid possesses  $31^2 = 961$  grid points. The matrix  $\mathbf{A}$  thus has 961 rows and 961 columns; or  $961^2 = 923,521$  elements (almost a million!). The solution of the linear equation  $\mathbf{A}s^{\ell+1} = \mathbf{R}$  may thus exceed the performance capabilities of a laptop for even the smallest ice-sheet modelling experiment.

Two approaches may be taken to overcome the difficulty imposed by the vast size of  $\mathbf{A}$ . The first is to use an iterative “relaxation” scheme to find the solution of the equation without ever having to store or factor the matrix  $\mathbf{A}$ . This is the approach Huybrechts (1992) used to investigate the evolution of the Antarctic ice sheet, for example, and is still used in the majority of ice-sheet models. It is based on the ADI-method, or Alternating-Direct-Implicit, in which the simple tridiagonal solution is sought for the  $i$ -direction to obtain a solution for ice thickness at an intermediate time step. The diffusion coefficients are then updated at this time step and a subsequent iteration solves the equation in the  $j$ -direction to obtain ice thicknesses on time step  $t + 1$ . We will not use this approach, sometimes leading to symmetry problems, but apply a direct matrix algorithm.

The direct matrix-solving approach takes advantage of the fact that  $\mathbf{A}$  has very few non-zero elements (Fig. 15). For our specific example, the matrix  $\mathbf{A}$  contains 4,325 non-zero elements of a total of 923,521 elements, which is approximately 0.47% of  $\mathbf{A}$ .

The Matlab code below shows the solution of the sparse matrix system using the indexing shown above. The resulting steady-state ice sheet is illustrated in Fig. 15.

```

for k=1:nsteps
    for j=1:jmax-1
        for i=1:imax-1
            d(i,j)=(1/4*(sn(i,j)+sn(i+1,j)+sn(i+1,j+1)+ ...
                        sn(i,j+1)))^5/(4*delta^2)*( ...
                        (sn(i+1,j)-sn(i,j)+sn(i+1,j+1)-sn(i,j+1))^2 ...
                        +(sn(i,j+1)-sn(i,j)+sn(i+1,j+1)-sn(i+1,j))^2);
        end
    end
    % construct the finite-difference stiffness matrix
    count=0;
    for j=2:jmax-1
        for i=2:imax-1
            count=count+1;
            row(count)=node(i,j);
            col(count)=node(i,j);
            value(count)=1/dt+1/delta^2*(d(i,j)+d(i-1,j)+d(i,j-1) ...
                +d(i-1,j-1));

            count=count+1;
            row(count)=node(i,j);
            col(count)=node(i,j+1);
            value(count)=-1/(2*delta^2)*(d(i,j)+d(i-1,j));

            count=count+1;
            row(count)=node(i,j);
            col(count)=node(i,j-1);
            value(count)=-1/(2*delta^2)*(d(i,j-1)+d(i-1,j-1));

            count=count+1;
            row(count)=node(i,j);
            col(count)=node(i+1,j);
            value(count)=-1/(2*delta^2)*(d(i,j)+d(i,j-1));

            count=count+1;
            row(count)=node(i,j);
            col(count)=node(i-1,j);
            value(count)=-1/(2*delta^2)*(d(i-1,j)+d(i-1,j-1));

            R(node(i,j))=1+sn(i,j)/dt;
        end
    end
    j=1;
    for i=2:imax-1
        count=count+1;
        row(count)=node(i,j);
        col(count)=node(i,j);
        value(count)=1;
        R(node(i,j))=0;
    end
    j=jmax;
    for i=2:imax-1
        count=count+1;
        row(count)=node(i,j);
        col(count)=node(i,j);

```

```

        value(count)=1;
        R(node(i,j))=0;
    end
    i=1;
    for j=2:jmax-1
        count=count+1;
        row(count)=node(i,j);
        col(count)=node(i,j);
        value(count)=1;
        R(node(i,j))=0;
    end
    i=imax;
    for j=2:jmax-1
        count=count+1;
        row(count)=node(i,j);
        col(count)=node(i,j);
        value(count)=1;
        R(node(i,j))=0;
    end
    count=count+1;
    row(count)=node(1,1);
    col(count)=node(1,1);
    value(count)=1;
    R(node(1,1))=0;

    count=count+1;
    row(count)=node(1,jmax);
    col(count)=node(1,jmax);
    value(count)=1;
    R(node(1,jmax))=0;

    count=count+1;
    row(count)=node(imax,jmax);
    col(count)=node(imax,jmax);
    value(count)=1;
    R(node(imax,jmax))=0;

    count=count+1;
    row(count)=node(imax,1);
    col(count)=node(imax,1);
    value(count)=1;
    R(node(imax,1))=0;

    % construct sparse matrix
    A=sparse(row,col,value);
    % Cholesky factor and solve
    s=A\R;
    for j=1:jmax;
        for i=1:imax
            sn(i,j)=s(node(i,j));
        end
    end
end
end

```

Exp	Variable	Benchmark	SIA model
FM	$h_{\text{summit}}$	$3419.90 \pm 1.70$	3421.82
	$q_{\text{midpoint}}$	$789.95 \pm 1.83$	790.43
MM	$h_{\text{summit}}$	$2997.5 \pm 7.4$	2986.41
	$q_{\text{midpoint}}$	$999.24 \pm 17.91$	994.49

Table 1: Comparison of our SIA model with the EISMINT-I fixed (FM) and moving margin (MM) experiment benchmark based on an ensemble of 2–3 models (Huybrechts et al, 1996) for the steady-state experiment.

### 3.6 EISMINT experiments

The EISMINT-I benchmark is the first series of ice-sheet model intercomparisons aiming at benchmarking large-scale ice sheet models under idealized and controlled conditions (Huybrechts et al, 1996). The first (fixed margin) experiment considers a square grid of  $1500 \times 1500$  km with a flat bed at zero elevation. Grid spacing is taken as  $\Delta = 50$  km leading to  $31 \times 31$  regularly-spaced grid points. Starting from zero ice thickness, the model is forced with a constant surface mass balance of  $0.3 \text{ m a}^{-1}$ . Further boundary conditions for the model are zero ice thickness at the edges of the domain. A constant value for the flow parameter of  $10^{16} \text{ Pa}^{-n} \text{ a}^{-1}$  is considered (Fig. 16).

The model described above is a 3d Type I model according to the classification scheme in EISMINT-I, i.e., diffusion coefficients for the grounded ice sheet are calculated on a staggered Arakawa-B grid. Table 1 lists the comparison with data from other 3d Type I models. Both ice thickness and flux compare very well within error bounds of the sample range (limited to only 2–3 models in the EISMINT-I benchmark, unfortunately).

The moving-margin experiment includes ice ablation, hence the presence of an equilibrium line on the ice sheet. This is obtained by defining the climatic conditions by  $\dot{a} = \min\{0.5, s(R_{\text{el}} - d_{\text{summit}})\}$ , where  $d_{\text{summit}}$  is here defined as the radial distance from the centre (in km), and  $s$  and  $R_{\text{el}}$  are  $10^{-2} \text{ m a}^{-1} \text{ km}^{-1}$  and 450 km, respectively (Huybrechts et al, 1996). The steady-state ice sheet according to this experiment does not reach the edge of the domain, but is circular in shape (Fig. 16).

Basic characteristics of the experiment are listed in Table 1, and simulated values of ice thickness ( $h_{\text{summit}}$ ) and ice flux between divide and margin are in good agreement with the benchmark.

### 3.7 A Greenland SIA ice sheet model

Another practical example to test a two-dimensional ice sheet model is to apply it to an existing ice sheet. Input for the model is present-day observed surface and bed topography and surface mass balance (Fig. 17). Data are spatially re-gridded on a horizontal grid with a spatial resolution of 20 km. The ice sheet model (similar to the example showed above) solves the SIA equations according to a diffusion equation. A simple nonlinear Weertman basal sliding law is added as a basal boundary condition. The grounded ice sheet is solved on a mask that represents the grounded terrain (above sea level). Ice thickness is kept to zero across the ocean and at the edges of the domain (Dirichlet boundary conditions).

The model is run forward for 20 000 years, starting from the present-day observed

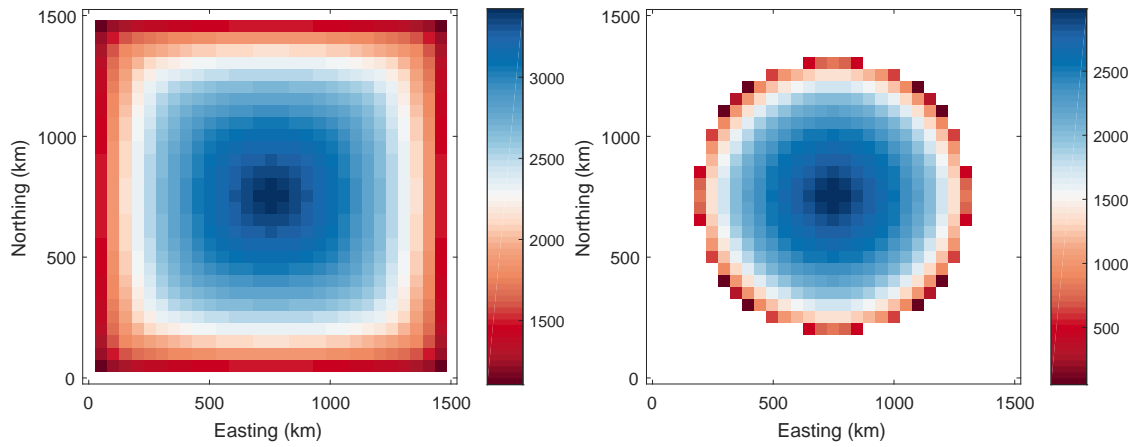


Figure 16: Modelled ice thickness according to the EISMINT-1 (left) and EISMINT-2 (right) experiments.

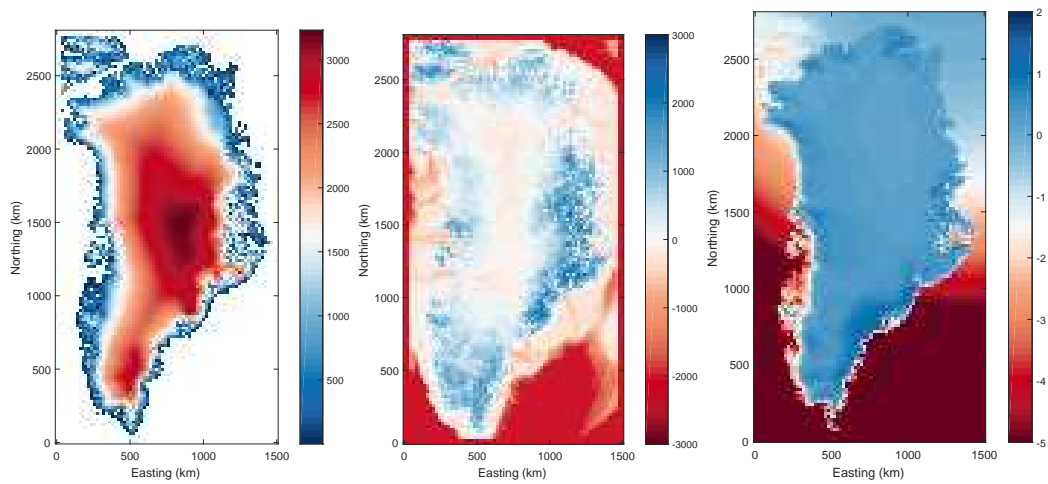


Figure 17: Observed surface topography (left), bedrock topography (centre) and surface mass balance (right) for the Greenland ice sheet on a spatial resolution of 20km.

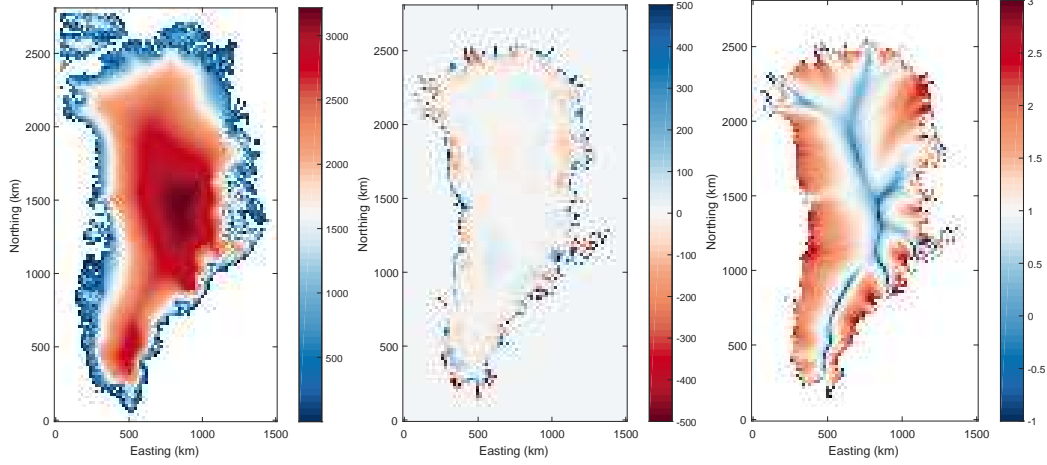


Figure 18: Steady-state modelled surface topography (left), difference between modelled and observed ice thickness (centre) and logarithmic vertical mean horizontal velocity (right) for the Greenland ice sheet on a spatial resolution of 20km after 20,000 years of integration, starting from present-day observed conditions.

surface topography and surface mass balance (as forcing field). A steady state ice sheet is obtained after approximately 10 000 years of forward integration (Fig. 18).

Even with a simple SIA model like this, a climate sensitivity study can be done. For this a surface temperature field is needed so that the surface mass balance can be forced by taking into account the mass balance - surface elevation feedback. Atmospheric forcing is applied in a parametrized way, based on the observed fields of precipitation (accumulation rate) and surface temperature. For a change in background (forcing) temperature  $\Delta T$ , corresponding fields of precipitation  $P$  and atmospheric temperature  $T_s$  are defined by (Huybrechts et al, 1998; Pollard and DeConto, 2012)

$$T_s = T_s^{\text{obs}} - \gamma(h_s - h_s^{\text{obs}}) + \Delta T, \quad (3.48)$$

$$P = \dot{a}^{\text{obs}} \times 2^{(T_s - T_s^{\text{obs}})/\delta T}, \quad (3.49)$$

where  $\gamma = 0.008^\circ\text{C m}^{-1}$  is the lapse rate and  $\delta T$  is  $10^\circ\text{C}$  (Pollard and DeConto, 2012). The subscript ‘obs’ refers to the present-day observed value. Any forcing (increase) in background temperature then leads to an overall increase in surface temperature corrected for elevation changes according to the environmental lapse rate  $\gamma$ . The parametrizations of  $T_s$  and  $P$  can easily be replaced by values that stem from GCMs, with appropriate corrections for surface elevation (e.g., de Boer et al, 2015).

Surface melt is parametrized using a positive degree-day model (Huybrechts and de Wolde, 1999). The total amount of positive degree days (PDD) is obtained as

$$\text{PDD} = \frac{1}{\sigma\sqrt{2\pi}} \int_0^A \left[ \int_0^{\bar{T}+2.5\sigma} T \exp\left(-\frac{(T - \bar{T})^2}{2\sigma^2}\right) dT \right] dt, \quad (3.50)$$

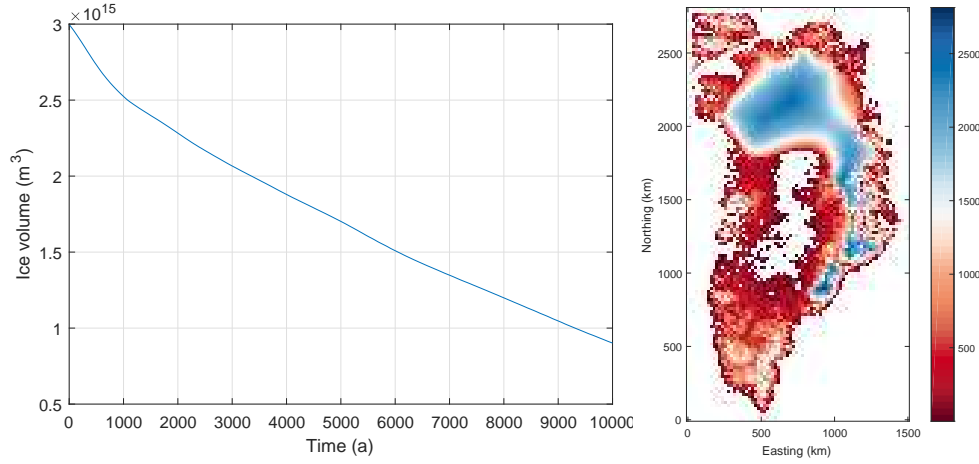


Figure 19: Evolution of the ice volume of the Greenland ice sheet when the SIA model is forced with a sudden background temperature change of  $\Delta T = +5^\circ\text{C}$ , correcting for the ice elevation-mass balance effect and using a PDD model for calculating surface melt (left). The right panel shows the ice sheet configuration after 60 000 years.

where  $\sigma$  is taken as  $5^\circ\text{C}$  (Reeh, 1989) and  $\bar{T}$  is the mean annual temperature. The annual number of positive degree days represents a melt potential, used to melt snow and (superimposed) ice. This is determined by applying a seasonal cycle to the atmospheric temperatures with a double amplitude of  $20^\circ\text{C}$ , linearly increasing to  $30^\circ\text{C}$  at an elevation of 3000 m, and kept at  $30^\circ\text{C}$  at higher elevations (Pollard and DeConto, 2012). The PDD melt potential is related to surface melt through a coefficient of 0.003 m of melt per degree day for melting snow and 0.008 for ice. As an example, we forced the Greenland steady-state model with a background temperature of  $\Delta T = +5^\circ\text{C}$  and ran the model for 60 000 years. The resulting ice volume change and the ice sheet at the end of the model run are shown in Fig. 19. The parametrizations used are very simple (based on present-day observed surface temperature and surface mass balance). Also the model is simple and not thermomechanically coupled (constant value of  $A$  in the constitutive equation). Results should therefore be taken with care (and not for granted), as these experiments are only to illustrate the concept of ice-sheet modelling in response to changes in climate.

## 4 Numerical modelling of ice shelves and ice streams (SSA)

### 4.1 Basic equations

We have derived the vertically integrated force balance equations according to the shallow-shelf approximation in Sect. 2.3,

$$\frac{\partial}{\partial x} \left( 2\eta h \left( 2\frac{\partial u}{\partial x} + \eta \frac{\partial v}{\partial y} \right) \right) + \frac{\partial}{\partial y} \left( \eta h \left( \frac{\partial u}{\partial y} + \eta \frac{\partial v}{\partial x} \right) \right) - \beta^2 u = \rho_i g h \frac{\partial s}{\partial x} \quad (4.1)$$

$$\frac{\partial}{\partial y} \left( 2\eta h \left( 2\frac{\partial v}{\partial y} + \eta \frac{\partial u}{\partial x} \right) \right) + \frac{\partial}{\partial x} \left( \eta h \left( \frac{\partial v}{\partial x} + \eta \frac{\partial u}{\partial y} \right) \right) - \beta^2 v = \rho_i g h \frac{\partial s}{\partial y} \quad (4.2)$$

The non-local definition of ice-shelf velocity is clear from the above equations. The solution to system is also a non-linear one, because the effective viscosity  $\eta$  is strain-rate dependent. In order to obtain a numerical solution, boundary conditions at the contact of the ice shelf with the ocean need to be determined, which is done in the following section.

## 4.2 Boundary conditions

The ice-shelf stress-equilibrium equations (4.1) and (4.2) require boundary conditions to be specified along the contour which defines the boundary to the ice-shelf domain. There are two types of boundary conditions: kinematic and dynamic. Kinematic conditions (specification of velocity) are usually applied where ice-shelves abut stagnant, at zero slip coastlines (such as where the Ross Ice Shelf abuts the Transantarctic mountains), or where ice streams flow into the ice shelf (in which case the velocity is specified from an examination of ice-stream dynamics). Dynamic conditions (specification of stress) are usually applied at the seaward, iceberg-calving front.

### 4.2.1 Kinematic conditions

Depth-averaged ice velocity is specified at all junctions with grounded ice or coastlines where the ice shelf shears past stagnant rock. Typically, ice flow into the ice shelf at grounding lines of ice sheets can have  $z$ -dependence which is incompatible with the  $z$ -independent horizontal flow of the ice shelf. The  $z$ -dependent structure of the input velocity is winnowed out of the net horizontal flow within a narrow transition zone between ice-sheet and ice-shelf flow regimes. This winnowing process is of little interest in most glaciological problems involving ice shelves. Thus, it is sufficient to ignore the winnowing process and simply specify the depth-averaged input velocity as the correct boundary condition.

### 4.2.2 Dynamic conditions

The balance of forces at the seaward ice front also introduces  $z$ -dependent structure in the ice-shelf flow which is winnowed away within a narrow transition zone extending inward from the ice front. This winnowing is of little interest, and may be safely ignored in the specification of boundary conditions for the ice-shelf stress-equilibrium equations. The balance of forces at the ice front which is relevant as a boundary condition is the depth-integrated balance:

$$\int_{-\frac{\rho_i}{\rho_w}h}^{(1-\frac{\rho_i}{\rho_w})h} \boldsymbol{\sigma} \cdot \mathbf{n} dz = -\frac{\rho_w g}{2} \left( \frac{\rho}{\rho_w} h \right)^2 \mathbf{n} \quad (4.3)$$



Here we have made use of the assumption that the ice shelf floats in hydrostatic equilibrium with seawater, i.e., that  $z_b = -\frac{\rho_i}{\rho_w}h$ , where  $\rho_w$  is the density of seawater. The pressure balance is illustrated in Fig. 1.

Deriving the boundary condition is straightforward and follows the previous analysis. Written in terms of stress components, the force balance obeys

$$\sigma_{xx}n_x + \sigma_{xy}n_y = \rho_w g z n_x \quad (4.4)$$

$$\sigma_{yx}n_x + \sigma_{yy}n_y = \rho_w g z n_y \quad (4.5)$$

Substituting for deviatoric stresses results in

$$(2\tau_{xx} + \tau_{yy})n_x + \tau_{xy}n_y = \rho_w g z n_x \quad (4.6)$$

$$\tau_{yx}n_x + (2\tau_{yy} + \tau_{xx})n_y = \rho_w g z n_y \quad (4.7)$$

We then apply the constitutive relationship and re-integrate the source term, i.e.,

$$\frac{1}{h} \left[ \int_0^{-\frac{\rho_i}{\rho_w}h} \rho_w g z dz + \int_{-\frac{\rho_i}{\rho_w}h}^{(1-\frac{\rho_i}{\rho_w})h} \rho g z dz \right] = \frac{1}{2} \rho g h \left( 1 - \frac{\rho_i}{\rho_w} \right) \quad (4.8)$$

Substituting for strain rates, hence velocity gradients, this results in

$$2\eta \left[ \left( 2\frac{\partial u}{\partial x} + \frac{\partial v}{\partial y} \right) n_x + \frac{1}{2} \left( \frac{\partial u}{\partial y} + \frac{\partial v}{\partial x} \right) n_y \right] = n_x \frac{1}{2} \rho g h \left( 1 - \frac{\rho}{\rho_w} \right) \quad (4.9)$$

$$2\eta \left[ \left( 2\frac{\partial v}{\partial y} + \frac{\partial u}{\partial x} \right) n_y + \frac{1}{2} \left( \frac{\partial u}{\partial y} + \frac{\partial v}{\partial x} \right) n_x \right] = n_y \frac{1}{2} \rho g h \left( 1 - \frac{\rho}{\rho_w} \right) \quad (4.10)$$

#### 4.2.3 Dynamic condition if $\mathbf{n} = \mathbf{n}_x$

As an illustration of how a dynamic boundary condition would be specified for an ice front that has an outward-pointing normal aligned with the  $x$ -axis (the ice front extends along the  $y$ -axis, and the ice shelf is to the left and the ocean to the right), i.e.,  $\mathbf{n} = \mathbf{n}_x$ . With this geometry,

$$\boldsymbol{\sigma} \cdot \mathbf{n}_x = (2\eta \dot{\varepsilon}_{xx} - p) \mathbf{n}_x \quad (4.11)$$

where  $p = \rho g(h - z) + 2\eta \dot{\varepsilon}_{zz}$  and (4.3) becomes

$$\int_{-\frac{\rho}{\rho_w}h}^{(1-\frac{\rho}{\rho_w})h} \boldsymbol{\sigma} \cdot \mathbf{n}_x dz = -\frac{\rho_w g}{2} \left( \frac{\rho}{\rho_w} h \right)^2 \mathbf{n}_x \quad (4.12)$$

To write the above dynamic condition in a form which involves  $u$  and  $v$ , we substitute for  $\mathbf{T}$  using the flow law and the definition of the deviatoric stress and then integrate over  $z$ . The integral of pressure over depth is evaluated as follows

$$\begin{aligned} \int_{-\frac{\rho}{\rho_w}h}^{(1-\frac{\rho}{\rho_w})h} p dz &= \int_{-\frac{\rho}{\rho_w}h}^{(1-\frac{\rho}{\rho_w})h} (\rho g(h - z) + 2\eta \dot{\varepsilon}_{zz}) dz \\ &= \rho g \frac{h^2}{2} - 2\eta h (\dot{\varepsilon}_{xx} + \dot{\varepsilon}_{yy}) \end{aligned} \quad (4.13)$$

where we have made use of the definition of pressure and the  $z$ -independence of the strain rates. Combining (4.11) and (4.13) with (4.3), we obtain

$$2\eta h (2\dot{\varepsilon}_{xx} + \dot{\varepsilon}_{yy}) = \frac{\rho g h^2}{2} \left(1 - \frac{\rho}{\rho_w}\right) \quad (4.14)$$

Making use of the definitions of the strain-rate components, we obtain the boundary condition:

$$2\eta h \left(2\frac{\partial u}{\partial x} + \frac{\partial v}{\partial y}\right) = \frac{\rho g h^2}{2} \left(1 - \frac{\rho}{\rho_w}\right) \quad (4.15)$$

### 4.3 Numerical solution of the SSA equations

The finite difference method gives a system of  $N$  equations and  $N$  variables, where  $N$  is the number of grid points. To approximate the equations, we solve a linear system, again making use of the sparsity of the matrices  $\mathbf{A}$  and  $\mathbf{C}$ .

$$\mathbf{A}(\mathbf{u}^\ell) \cdot \mathbf{u}^{\ell+1} = \mathbf{b}(\mathbf{u}^\ell) \quad (4.16)$$

$$\mathbf{C}(\mathbf{v}^\ell) \cdot \mathbf{v}^{\ell+1} = \mathbf{d}(\mathbf{v}^\ell) \quad (4.17)$$

where  $\ell$  is the iteration number,  $\mathbf{A}$  and  $\mathbf{C}$  are the coefficient matrices, which are very sparse. The equations are solved using **sparse matrix algorithms** based on the conjugate gradient method. However, an iteration scheme is necessary, because the viscosity term is still a function of  $u, v$ . We therefore use a simple sequential update (Picard iteration):

1.  $c \leftarrow 0$
2. repeat until error < tolerance
3.  $\eta \leftarrow \text{compute\_viscosity}(u, v)$
4.  $u^{\ell+1} \leftarrow \text{compute\_u\_component}(v^\ell, \eta)$
5.  $v^{\ell+1} \leftarrow \text{compute\_v\_component}(u^{\ell+1}, \eta)$

### 4.4 Example of an ice-shelf model

In the following we test the two-dimensional ice shelf equations for a simplified geometry. We consider a square ice shelf of constant ice thickness that is bounded at three lateral sides by a grounded (non-moving) ice sheet. This is the kinematic boundary as defined above. On the fourth lateral side we apply a dynamic boundary, which is the contact with the ocean. In the experiment, the ice shelf is perfectly floating and flat, so that the driving stress is everywhere zero. At the ocean side, the seawater pressure will balance the ice pressure, which will make the ice flow.

The velocities are calculated on a staggered grid. The grid is similar to the one used in Fig. 14, where the local slope components  $\partial s / \partial x, \partial s / \partial y$  are calculated on a grid that is different from the grid of  $s$ . This means that two different grids are employed for the  $u$  and  $v$  velocities. The effective viscosity is calculated on the standard  $h$  grid (or  $s$ -grid in Fig. 14).

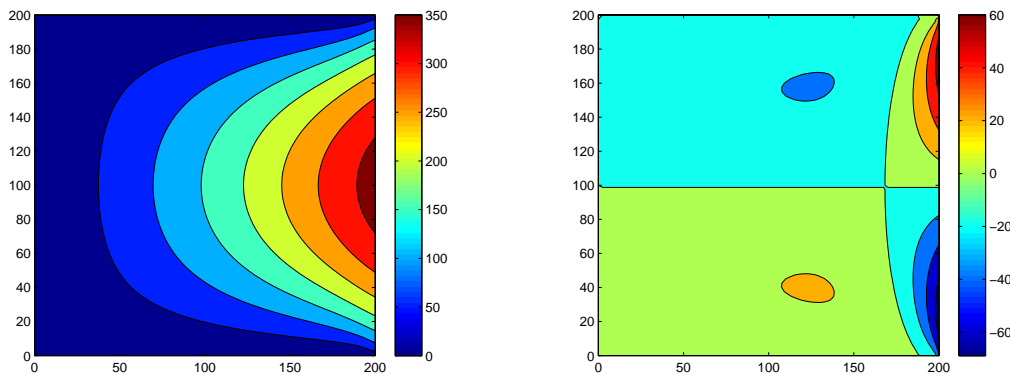


Figure 20: Components of the  $u$  velocity (left) and  $v$  velocity (right) for the experiment with a constant effective viscosity.

The first example is a simplified version of the ice-shelf equations, in which we keep the effective viscosity constant. In this case, the solution of the flow field does not require an iterative solution. However, the numerical scheme used first calculates the  $u$  velocities and subsequently determines the  $v$  velocities, which will require an iteration. The two components of the velocity are displayed in Fig. 20.

The second example shows the velocity distribution when the effective viscosity is made a function of strain rates (Fig. 21).

In a final example, we define an ice stream coming in at the upstream boundary, defined by a Gaussian function. The result is shown in Fig. 22.

## 5 Numerical modelling of marine ice sheets

### 5.1 Marine ice-sheet instability

The concept of MISI (Fig. 23B), first proposed 40 years ago (Weertman, 1974; Thomas and Bentley, 1978), provided a basis to hypothesize a possible collapse of West Antarctica as a consequence of anthropogenic global warming (Mercer, 1978). However, the MISI theory was challenged by Hindmarsh (1996), considering that ice shelves were too weak (and therefore mechanically uncoupled from the ice sheet) to affect the force balance of the grounded ice sheet. This led to the hypothesis of neutral equilibria that were neither stable or unstable (Hindmarsh, 1996). The resulting non-uniqueness of numerically-derived ice-sheet profiles, and the failure to recognise the importance of model resolution, confounded attempts to reproduce consistent dynamical behaviour among different models (Vieli and Payne, 2005). MISI theory was also disputed by observations of an apparently balanced ice sheet, but that was before several ice shelves collapsed in the Antarctic Peninsula, leading to increased glacier discharge (Scambos et al, 2004), and glaciers started to retreat in the Amundsen Sea Embayment (ASE; Rignot, 1998; Wingham et al, 1998; Shepherd et al, 2002).

More recently, the concept of Marine Ice Cliff Instability (MICI; Fig. 23B) has emerged (Pollard et al, 2015; DeConto and Pollard, 2016), i.e., that ice cliffs become

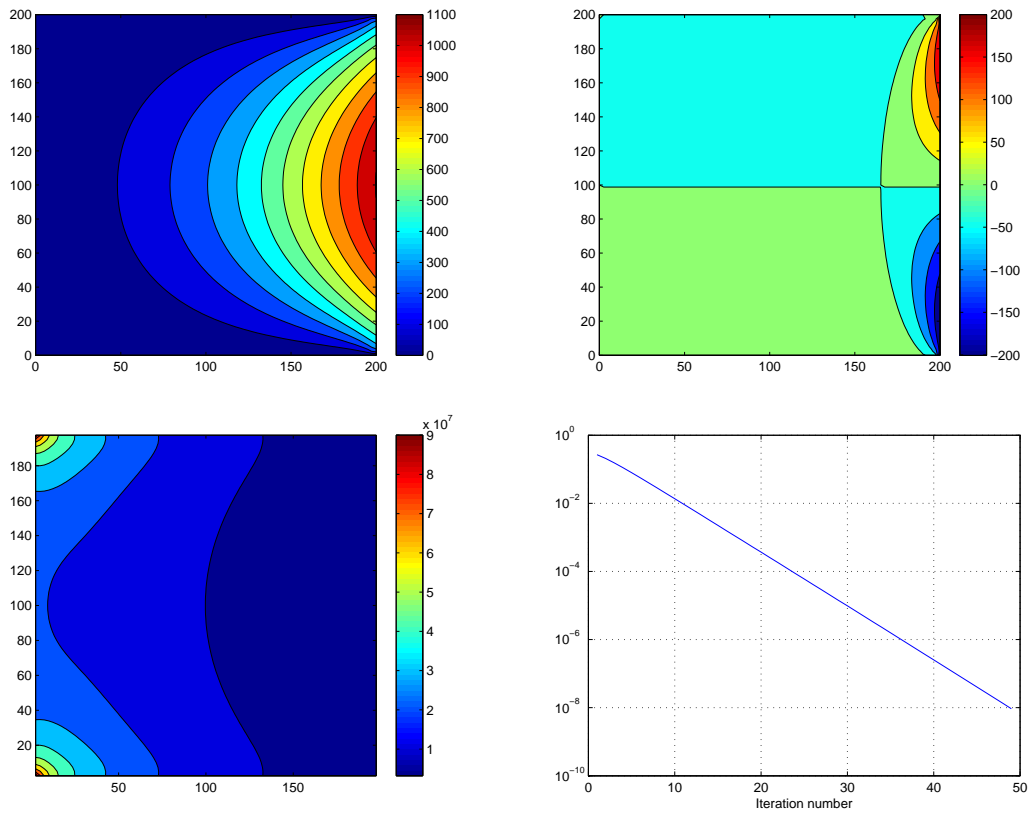


Figure 21: Components of the  $u$  velocity (top left) and  $v$  velocity (top right) for the experiment with a strain-dependent effective viscosity. The bottom panels display the effective viscosity (bottom left) and the iteration error (bottom right).

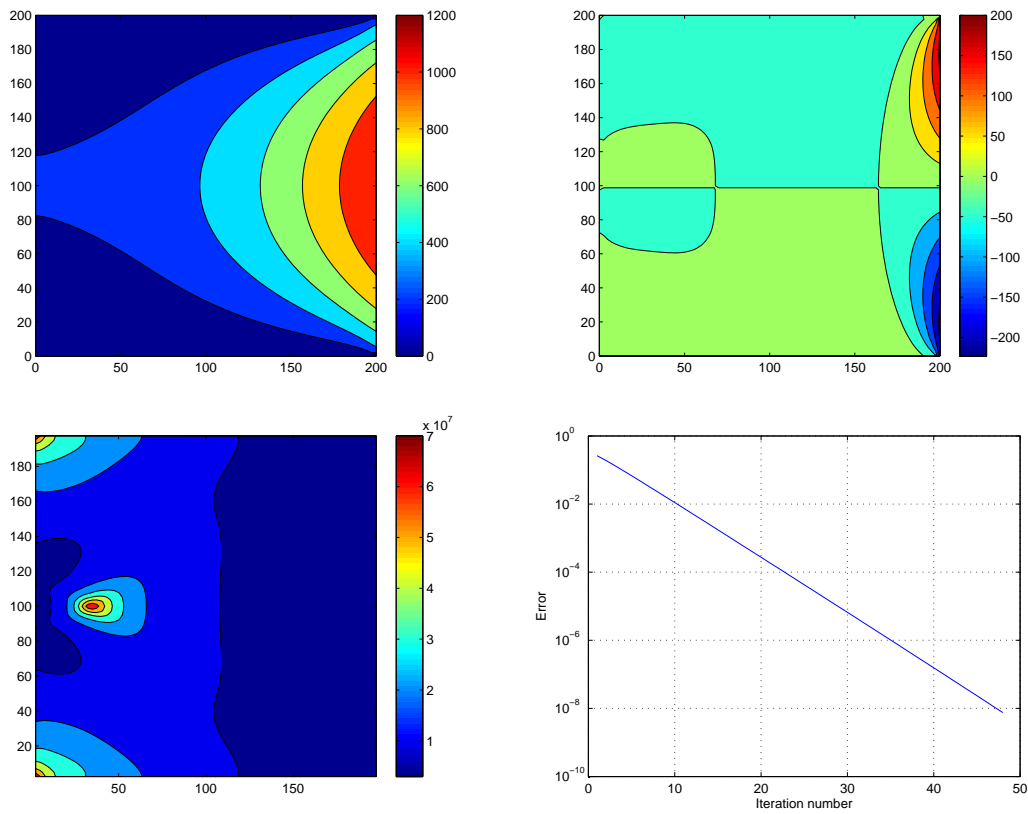


Figure 22: Components of the  $u$  velocity (top left) and  $v$  velocity (top right) for the experiment with a strain-dependent effective viscosity and an ice stream entering the upstream part of the ice shelf. The bottom panels display the effective viscosity (bottom left) and the iteration error (bottom right).

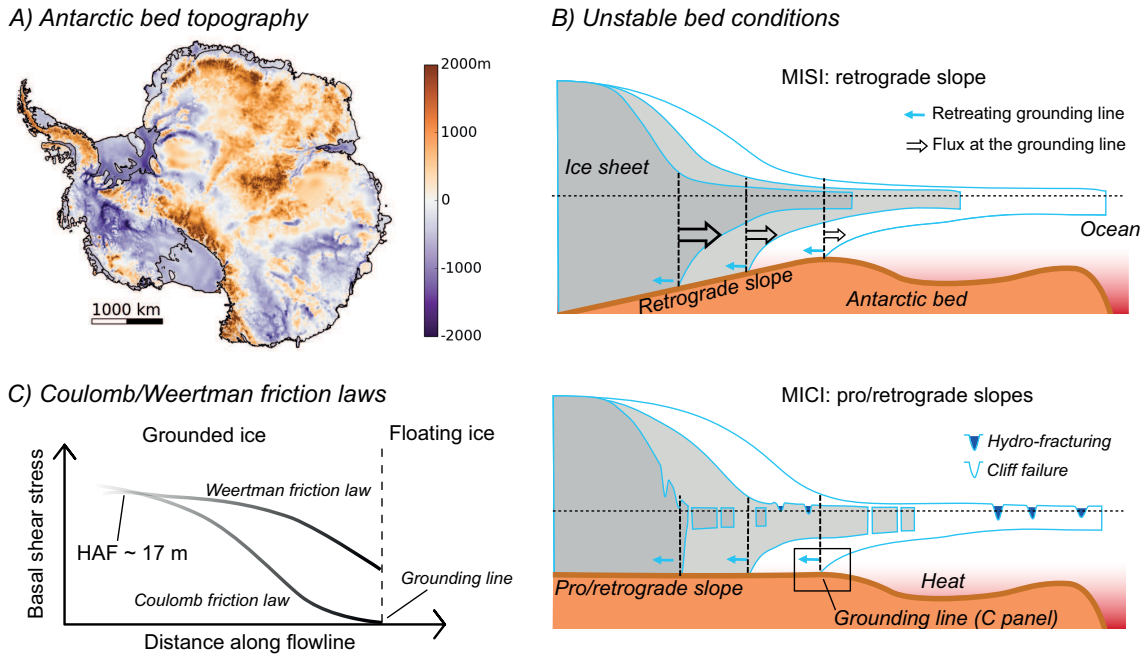


Figure 23: (A) Antarctic bed topography (Bedmap2; Fretwell et al, 2013). (B) Depiction of MISI (top) and MICI (bottom). Ice discharge generally increases with increasing ice thickness at the grounding line. For a bed sloping down towards the interior this may lead to unstable grounding-line retreat (MISI), as increased flux (for example, due to reduced buttressing) leads to thinning and eventually flotation, which moves the grounding line into deeper water where the ice is thicker. Thicker ice results in increased ice flux, which further thins (and eventually floats) the ice, which results in further retreat into deeper water (and thicker ice), and so on. MICI is the result of collapse of exposed ice cliffs (after the ice shelf collapses due to hydro-fracturing) under their own weight. MISI applies for a retrograde slope bed, while MICI can also apply for prograde slopes. Both MISI and MICI are thus superimposed for retrograde slopes. The square indicates a subset shown in (C). The red colour beneath the ice shelf suggests that the deeper the ice the higher it is subjected to melt and grounding-line retreat (after DeConto and Pollard, 2016). (C) Schematic showing the difference in basal shear stress obtained with Weertman and Coulomb friction laws at the grounding line, respectively (after Tsai et al, 2015). The two friction laws result in a similar shear stress for a height-above-flotation (HAF) above 17 m (Tsai et al, 2015).

unstable and fall down if higher than  $\sim 90$  m above sea level, leading to the collapse of ice sheets during past warm periods (DeConto and Pollard, 2016). MICI is a process that facilitates and enhances Marine Ice Sheet Instability (MISI; Fig. 23B for more details) through a decrease in ice-shelf buttressing. MICI relies on the assumption of perfect plastic rheology to represent failure. Cliff instability requires an *a priori* collapse of ice shelves, and is favoured by hydro-fracturing through the increase of water pressure in surface crevasses, which increases the opening term (Bassis and Walker, 2012; Nick et al, 2013; Pollard et al, 2015). Contrary to MISI, MICI can also occur on prograde bed slopes.

## 5.2 Schoof's boundary layer theory

Schoof (2007) gave mathematical formulation of the MISI theory put forward by Weertman (1974), dispelling the idea that ice sheets and ice shelves are mechanically uncoupled. This theory showed that the ice-sheet margin should be treated as a moving boundary problem that requires two constraints, i.e. a hydrostatic floatation constraint and a flux constraint that satisfies the momentum balance for ice-sheet and ice-shelf flow (mechanical coupling). Therefore, to accurately capture grounding line migration, it is necessary to resolve the transition zone at a sufficiently fine resolution. Schoof (2007) proposed a semi-analytical solution for the ice flux across the grounding line  $q_g$  obeying both boundary conditions.

If we consider the SSA along a flowline, the stress balance can be simplified to

$$\frac{\partial}{\partial x} \left( -4\eta h \frac{\partial u}{\partial x} \right) + \tau_b = \rho g h \frac{\partial h}{\partial x} \quad (5.1)$$

where the effective viscosity is defined by

$$\eta = \frac{1}{2} A^{-1/n} \left( \frac{\partial u}{\partial x} \right)^{\frac{1}{n}-1} \quad (5.2)$$

with the following definition for the basal shear stress (simplified to the driving stress):

$$\tau_b = C u^{1/m} \approx \rho g h \frac{\partial h}{\partial x} \quad (5.3)$$

The ice flux  $q = uh$  is further considered constant near the grounding line. This is acceptable if we consider a narrow zone across the grounding line, so that  $\frac{\partial q}{\partial x} \approx 0$ , or

$$\frac{\partial u}{\partial x} h + \frac{\partial h}{\partial x} u = 0 \Rightarrow \frac{\partial u}{\partial x} = -\frac{q}{h^2} \frac{\partial h}{\partial x} \quad (5.4)$$

The above equations can now be combined with a friction law, which is written as

$$\frac{\partial u}{\partial x} = -\frac{C}{\rho g} \frac{q^{1+1/m}}{h^{3+1/m}} \quad (5.5)$$

The boundary condition with the ocean can then be combined with  $\eta$  to yield the following expression:

$$4\eta h \frac{\partial u}{\partial x} = 2A^{-1/n} h \left( \frac{\partial u}{\partial x} \right)^{1/n} = \frac{1}{2} \rho g h^2 \left( 1 - \frac{\rho}{\rho_w} \right) \quad (5.6)$$

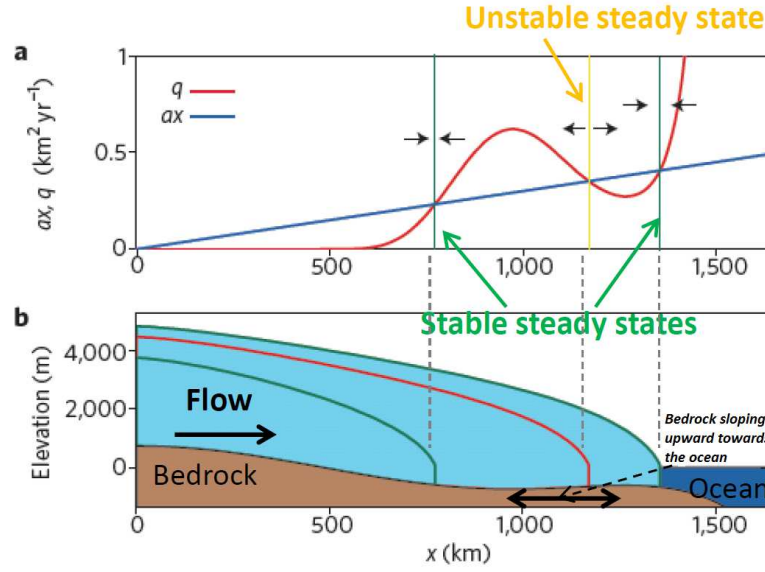


Figure 24: Analysis of steady-state grounding-line positions as a function of bed slope (after Schoof (2007)).

which in combination with the friction law leads to an expression of flux  $q$  at the grounding line

$$q_g = \left( \frac{A(\rho g)^{n+1}(1 - \rho/\rho_w)^n}{4^n C} \right)^{\frac{m}{m+1}} h_g^{\frac{m(n+3)+1}{m+1}} \quad (5.7)$$

where  $A$  is the depth-averaged parameter in Glen's flow law,  $n$  is the Glen's flow law exponent,  $C$  is the basal friction coefficient,  $m$  is the basal friction exponent, and  $h_g$  is the ice thickness at the grounding line. This implies that ice flux at the grounding line is sensitive to changes in the ice shelf, contrary to earlier findings by Hindmarsh (1993). Moreover, for  $m = 3$  and  $n = 3$ , the flux  $q_g$  scales to  $h_g^{4.75}$ .

In absence of lateral buttressing, unique and stable grounding line equilibrium positions are found on downsloping bed slopes (slopes that negative in the direction of the ice flow; Fig. 24). However, unstable equilibria exist on upsloping or retrograde bed slopes, meaning that no steady-state positions can occur.

### 5.3 A flowline ice-stream SSA model with grounding line

We consider an ice stream system in contact with the ocean along a flow-line. We start our analysis with the SSA force balance in  $x$  (2.38) and neglect all variations in  $y$ . This is called the principle of plain strain, i.e.,

$$4 \frac{\partial}{\partial x} \left( \eta h \frac{\partial u}{\partial x} \right) - \beta^2 u = \rho_i g h \frac{\partial s}{\partial x} \quad (5.8)$$

where the effective viscosity  $\eta$ , neglecting lateral strain rates, becomes



$$\begin{aligned}
\eta &= \frac{1}{2} A^{-1/n} \dot{\varepsilon}^{\frac{1-n}{n}} \\
&= \frac{1}{2} A^{-1/n} \left( \dot{\varepsilon}_{xx}^2 \right)^{\frac{1-n}{2n}} \\
&= \frac{1}{2} A^{-1/n} \left| \frac{\partial u}{\partial x} \right|^{\frac{1-n}{n}}
\end{aligned} \tag{5.9}$$

and where  $\beta^2$  is the basal friction of the ice stream. The value is represented as a squared value, since it should always be positive in the force balance, as  $\sigma_b$  needs to take the sign of  $u$ . The basal friction  $\beta^2$  is not necessarily constant, but can be a function of local till characteristics, basal temperature and the velocity  $u$  itself, the latter when the sliding velocity takes the form of a plastic (and not a viscous) sliding law.  $\beta^2 = 0$  for the floating ice shelf. For a plastic sliding law according to

$$u_b = A_s \tau_b^m \tag{5.10}$$

the value of  $\beta^2$  in the ice stream is then defined as

$$\beta^2 = A_s^{-1/m} |u|^{1/m-1} \tag{5.11}$$

where  $m = 3$  (Schoof, 2007).

## 5.4 Numerical solution to the ice-stream model

### 5.4.1 Velocity field

We discretize (5.8) and (5.9) on a staggered grid, where the  $u$ -velocities are inbetween grid points ( $u_i$  lying between  $H_i$  and  $H_{i+1}$ ). The effective viscosity  $\eta$  is calculated on the  $h$ -grid. By definition, we then have:

$$\eta_i = \frac{1}{2} A^{-1/n} \left| \frac{u_{i+1} - u_i}{\Delta x} \right|^{\frac{1-n}{n}} \tag{5.12}$$

The discretization of (5.8) then becomes

$$\begin{aligned}
&u_{i-1} \left\{ \frac{2(\eta_i h_i + \eta_{i+1} h_{i+1})}{(\Delta x)^2} - \frac{\eta_{i+1} h_{i+1} - \eta_{i-1} h_{i-1}}{(\Delta x)^2} \right\} \\
&\quad + u_i \left\{ -\frac{4(\eta_i h_i + \eta_{i+1} h_{i+1})}{(\Delta x)^2} - \beta_i^2 \right\} \\
&+ u_{i+1} \left\{ \frac{2(\eta_i h_i + \eta_{i+1} h_{i+1})}{(\Delta x)^2} + \frac{\eta_{i+1} h_{i+1} - \eta_{i-1} h_{i-1}}{(\Delta x)^2} \right\} \\
&= \rho g \left( \frac{h_i + h_{i+1}}{2} \right) \frac{s_{i+1} - s_i}{\Delta x}
\end{aligned} \tag{5.13}$$

This is again a tridiagonal system of equations that can be solved by the methods seen previously. Note that the effective viscosity  $\eta$  is still a function of velocity  $u$ , so that this

system needs to be solved iteratively. First estimate  $u^{(0)}$ , then calculate  $\eta$  based on these estimates solve the tridiagonal system for  $u^{(1)}$  based on  $\eta^{(0)}$ ; calculate  $\eta^{(1)}$  based on  $u^{(1)}$ , etc. until convergence is reached. In general, only a few iterations are necessary.

In the following example we will consider a flow-line stretching from the ice divide to the ocean. Boundary conditions for the velocity at the ice divide are  $u_1 = 0$ . At the seaward edge we derive the force balance from (4.15), where gradients in the  $v$ -velocity are neglected, i.e.,

$$\begin{aligned} 2\eta h \left( 2 \frac{\partial u}{\partial x} \right) &= \frac{\rho g h^2}{2} \left( 1 - \frac{\rho}{\rho_w} \right) \\ 2^{-1/n} h \left| \frac{\partial u}{\partial x} \right|^{\frac{1-n}{n}} \frac{\partial u}{\partial x} &= \frac{\rho g h^2}{2} \left( 1 - \frac{\rho}{\rho_w} \right) \\ \frac{\partial u}{\partial x} &= A \left[ \frac{\rho g h}{4} \left( 1 - \frac{\rho}{\rho_w} \right) \right]^n \end{aligned} \quad (5.14)$$

A numerical solution for the velocity on the last grid point is then given by:

$$u_N = u_{N-1} + A \left[ \frac{\rho g h_N}{4} \left( 1 - \frac{\rho}{\rho_w} \right) \right]^n \Delta x \quad (5.15)$$

The upper boundary conditions is a stress-free surface, which is already included in the derivation of the force balance. At the lower boundary, conditions depend on the floatation criterion for ice, given by

$$h^* = b - Z_{\text{sealevel}} + h \frac{\rho_i}{\rho_w} \quad (5.16)$$

where  $Z_{\text{sealevel}}$  is the sea-level elevation with respect to the used datum. The ice stream is grounded for  $h^* > 0$  and floated otherwise. The lower boundary condition then reads

$$\begin{aligned} \beta^2 &= A_s^{-1/m} u^{1/m-1} \quad \text{for } h^* > 0 \\ \beta^2 &= 0 \quad \text{for } h^* \leq 0 \end{aligned}$$

### 5.4.2 Continuity equation

For ice streams and ice shelves, the continuity equations is not written as a diffusive equation but kept purely advective, so that,

$$\frac{\partial h}{\partial t} = \dot{a} - \frac{\partial}{\partial x}(uh) \quad (5.17)$$

For a semi-implicit scheme with  $u$  velocities on a staggered grid, the discretization of (5.17) becomes

$$h_{i,t+1} + \frac{(h_{i+1,t+1} + h_{i,t+1})u_i - (h_{i,t+1} + h_{i-1,t+1})u_{i-1}}{2\Delta x} = h_{i,t} + \dot{a}_i \Delta t \quad (5.18)$$

which is again solved as a tridiagonal system.

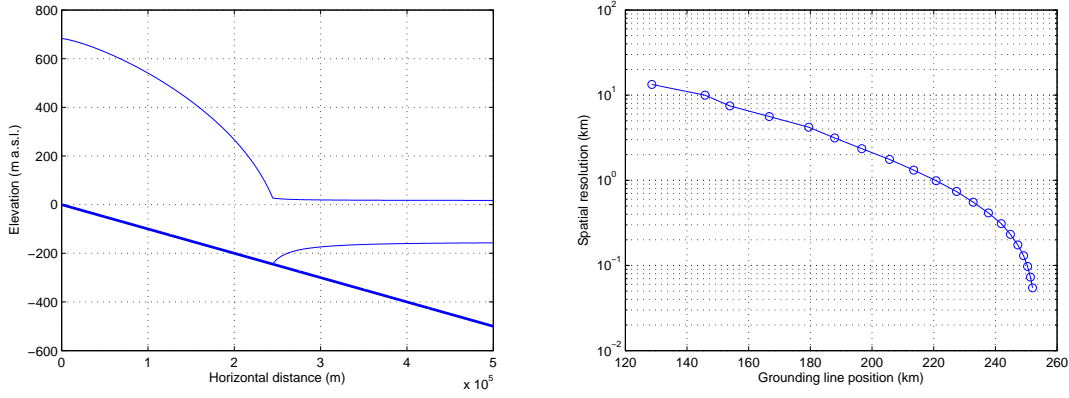


Figure 25: Left: surface, ice bottom and bedrock profiles for the ice stream and ice shelf according to the numerical model. Spatial discretization was taken as 250 m. Right: steady-state grounding line position as a function of spatial model resolution.

### 5.4.3 Example

We define a linearly-sloping bed along our flow-line, defined by  $b(x) = x^{-1}$ , where  $x$  is the horizontal distance (in km) and  $b$  the bed elevation (m a.s.l.). Fig. 25 shows the steady-state profile of an ice-stream/ice-shelf system according to the numerical model. In this experiment, the spatial resolution was taken as 250m. Grounding-line models require a high spatial resolution to resolve the grounding line. As shown in Schoof (2007) and further discussed in Pattyn et al (2013), to resolve the grounding line, longitudinal stress gradients need to be computed at **both** sides (upstream and downstream) of the grounding line. Since they are active at length scales that are smaller than the ice thickness  $Lg < Hg$ , this requires a high spatial resolution. Some methods have been developed to overcome this, by implementing directly the solution due to Schoof (5.7) in the ice stream model, based on a heuristic rule (Pollard and DeConto, 2009; Docquier et al, 2011; Pattyn, 2017).

## 5.5 MISMIP experiments

Vieli and Payne (2005) showed that marine ice sheet finite difference models were highly sensitive to horizontal grid size. Large grid sizes, for instance, prevent grounding line migration. Only small enough grid sizes lead to grounding line advance (Huybrechts et al, 1998; Vieli and Payne, 2005; Durand et al, 2009) and Pattyn et al (2012) has demonstrated that spatial resolution should be other order of  $< 500$  m. We compare our model results to the semi-analytical solution derived by Schoof (2007).

The first experiment is a MISMIP variant<sup>1</sup> (Pattyn et al, 2012). A steady state geometry is developed on a linearly downward-sloping bedrock defined by

$$b(x) = -100 - x, \quad (5.19)$$

<sup>1</sup>MISMIP: Marine Ice Sheet Model Intercomparison Project; <http://homepages.ulb.ac.be/~fpattyn/mismip/>

Table 2: Constants and parameter settings for the MISMIP experiments

Parameter	Description	Value	Unit
$\rho_i$	Ice density	900	$\text{kg m}^{-3}$
$\rho_w$	Water density	1000	$\text{kg m}^{-3}$
$g$	Gravitational acceleration	9.8	$\text{m s}^{-2}$
$n$	Glen's flow law exponent	3	
$a$	Accumulation rate	0.3	$\text{m a}^{-1}$
$L$	Domain length	1000	km
$C$	Basal friction coefficient	$10^7$	$\text{Pa s}^m \text{m}^{-m}$
$m$	Basal friction exponent	3	

where  $b$  is bedrock elevation (m a.s.l.) and  $x$  is distance from the ice divide (km). Other parameters and constants are given in Table 2. In the standard experiment, a value for Glen's flow law parameter of  $A = 10^{-25} \text{ Pa}^{-n} \text{ s}^{-1}$  is used. A steady state is achieved after  $\sim 40\,000$  years of integration. Starting from this steady state configuration (further addressed to as **initial** state), the value for  $A$  is decreased (increasing viscosity), leading to an advance of the grounding line. This process is repeated for subsequent changes in  $A$ , ranging from  $10^{-25}$  to  $10^{-26}$  in steps of  $2 \times 10^{-26}$ , as well as the reverse process (starting from  $A = 10^{-26}$  and decreasing the viscosity in steps of  $2 \times 10^{-26}$ ). Each of these step changes takes  $\sim 20\,000$  years to reach a steady state. What is referred to below as **final** state, is the steady state after complete advance and retreat and for the value of  $A = 10^{-25} \text{ Pa}^{-n} \text{ s}^{-1}$ .

The second experiment corresponds to MISMIP Experiment 3a, where a steady state geometry is allowed to develop on an overdeepened polynomial bedrock, defined by

$$b(x) = 729 - 2184.8 \times \left(\frac{x}{750 \text{ km}}\right)^2 + 1031.72 \times \left(\frac{x}{750 \text{ km}}\right)^4 - 151.72 \times \left(\frac{x}{750 \text{ km}}\right)^6. \quad (5.20)$$

The flow parameter  $A$  is varied stepwise between  $3 \times 10^{-25}$  and  $2.5 \times 10^{-26} \text{ Pa}^{-n} \text{ s}^{-1}$ . Other parameters are similar to those of the previous experiment, except for the domain length, taken as  $L = 1800 \text{ km}$  and the basal sliding parameter set to  $C = 7.624 \times 10^6 \text{ Pa s}^m \text{m}^{-m}$ .

A major drawback of the Schoof solution is its validity restricted to steady state solutions and not to transient states. However, grounding line migration rate is a major issue when trying to understand marine ice sheet response over decadal time scales (as needed in IPCC projections). The transient response of the grounding line should therefore be independent of numerical parameters, such as grid resolution and time step, and should be coherent with theoretical developments.

Figure 26 shows the steady state profiles of the ice sheet and ice shelf along the flow-line for both the linearly downward-sloping and the overdeepened bedrock profiles (staggered SSA model). Grounding line advance is obtained when decreasing the value of  $A$ , and a retreat is invoked when  $A$  is increased to its initial value. Advance and retreat steady

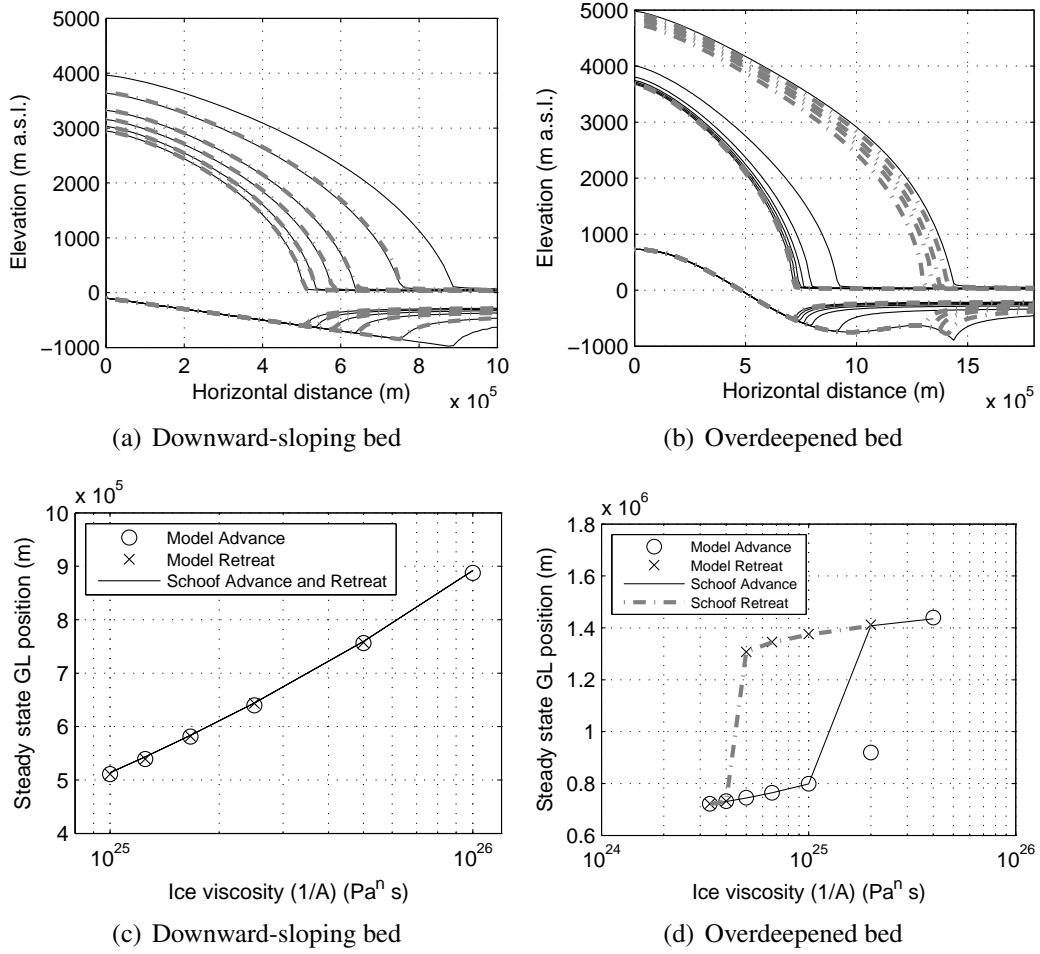


Figure 26: Steady state profiles (solid black curve: advance; dashed gray curve: retreat) of the ice sheet on a downward-sloping bed (a and c) and on an overdeepened bed (b and d) for the SSA model on a staggered grid (first and second experiments).

state profiles are hardly discernible, as both are lying close together. According to theory (Schoof, 2007), they should overlap, which defies neutral equilibrium of grounding line positions.

## 5.6 Evaluating the buttressing effect of ice shelves

Ice shelves are the prime gatekeepers of Antarctic continental ice discharge. The breakup of the Larsen B ice shelf and the subsequent speed-up of outlet glaciers that previously discharged into the ice shelf witness this important instability mechanism (Scambos et al, 2000, 2004). In West Antarctica, observational evidence (Rignot et al, 2014) as well as modelling studies (Favier et al, 2014; Joughin et al, 2014; Seroussi et al, 2014) show that the reduction in buttressing of ice shelves in the Amundsen Sea embayment may lead to significant inland ice mass loss, and that unstoppable retreat of the grounding line of Thwaites Glacier may already be on its way (Joughin et al, 2014).

Since ice shelf buttressing is a key element in the stability of the Antarctic ice sheet, a useful experiment to understand underlying model buttressing physics is the sudden

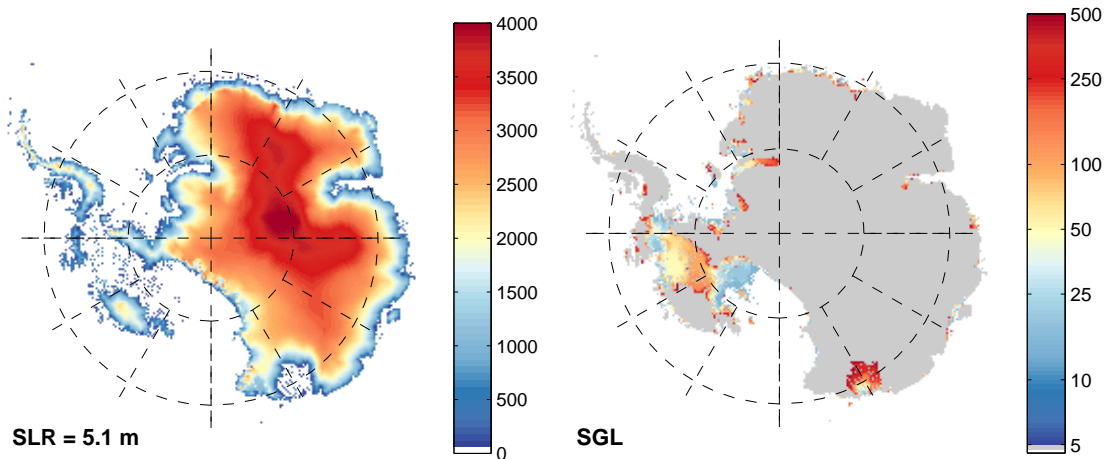


Figure 27: Left: Grounded ice sheet surface elevation (m a.s.l.), 500 years after sudden removal of all ice shelves. Right: grounding-line position in time according to the same experiment (colour scale is nonlinear and represents time in years). SLR denotes the contribution to sea level rise after 500 years (Pattyn, 2017).

removal of all floating ice shelves, starting from the initialized model state, and to let the model evolve over time. Over this period ice shelves were not allowed to regrow, which is equivalent to removing all floating ice at each time step. This experiment was carried out with the f.ETISh (fast Elementary Thermomechanical Ice Sheet) model, using a hybrid ice-sheet/ice-shelf model (type L1L1\*) and initialized to present-day ice sheet conditions (steady-state ice sheet with surface topography close to observed and optimized basal friction field). The spatial resolution of the model is 25 km, which requires a parametrised flux condition at the grounding line (according to Schoof (2007)) to cope with grounding-line migration on coarse grids (Pattyn, 2017). The experiment results in a sudden ice-mass loss and grounding-line retreat, whereby the West Antarctic ice sheet collapses entirely in less than 200 years (Fig. 27).

## 6 Conclusions

Over the last decades, ice sheet modelling has seen a tremendous evolution, from large-scale SIA models (Huybrechts, 1992) to complex full-Stokes models, such as Elmer/Ice (Gillet-Chaulet et al, 2012), and several approximations to the Stokes equations as illustrated in this course. Different ice-sheet models of varying complexity are now freely available for use (BISICLES, CISM, Elmer/Ice, ISSM, PISM, SICOPOLIS, ...). The easier access to models removes the barrier for using them and opens them up to a wider community. This is definitely a positive evolution, but has a number of pitfalls, as the choice of a model is often not based on the precise knowledge of the limits of a particular model or model code.

Complex models not necessarily better models. For instance, applying a FS model (or equivalent Blatter–Pattyn model) to an ice sheet or ice cap on a grid size of tens of kilometres will virtually yield the same result as using a SIA model, especially if sliding

is limited to the margins. This is because SIA is perfectly valid under these large-scale conditions (and aspect ratios) and membrane stresses will have a limited effect. Spatial resolution is crucial in ice sheet modelling in order to capture processes that require such scale. Especially for marine boundaries (grounding lines) high spatial resolution is required (<500 m), which led some models to use adaptive grid techniques or finer meshing based on finite elements to overcome this (BISICLES, Elmer/Ice).

Time scales are also important. At longer time scales (hundreds of years to millennia), thermomechanical effects may play a significant role and thermomechanical coupling should be considered. Also, boundary conditions should be carefully analysed and taken into account properly. They can be extremely problem-dependent (and not universal as build-in into a particular ice-sheet model). Therefore, the choice of model is function of what problem you want to study. As an example, for many glaciers with limited sliding and a simple geometry, surface mass balance may well be dominant over the dynamic contribution of the glacier to the global mass balance. If one studies the effect of climate on such a glacier, a glacier model is maybe not the most adapted tool.

Finally, interpretation of model results should be done with great care and always as a function of the approximations made and boundary conditions chosen.

## Acknowledgments

These notes are based on a collation of several sources, such as review papers (Docquier et al, 2011; Pattyn et al, 2017) and my own coursework at the ULB. The section on the approximations to the Stokes equations has been largely inspired on the work by Isabel Nias (PhD thesis), the section on the two-dimensional ice sheet stems from MacAyeal (1997) and the model for ice shelves has been in part taken from MacAyeal (1997) and Rommelaere and Ritz (1996).

## References

- Bassis JN, Walker CC (2012) Upper and lower limits on the stability of calving glaciers from the yield strength envelope of ice. *Proceedings of the Royal Society of London A: Mathematical, Physical and Engineering Sciences* 468(2140):913–931, DOI 10.1098/rspa.2011.0422
- Blatter H (1995) Velocity and stress fields in grounded glaciers: a simple algorithm for including deviatoric stress gradients. *J Glaciol* 41(138):333–344
- de Boer B, Dolan AM, Bernalles J, Gasson E, Goelzer H, Golledge NR, Sutter J, Huybrechts P, Lohmann G, Rogozhina I, Abe-Ouchi A, Saito F, van de Wal RSW (2015) Simulating the antarctic ice sheet in the late-pliocene warm period: Plismip-ant, an ice-sheet model intercomparison project. *The Cryosphere* 9(3):881–903, DOI 10.5194/tc-9-881-2015
- Bueler E, Brown J (2009) Shallow shelf approximation as a 'sliding law' in a thermomechanically coupled ice sheet model. *Journal of Geophysical Research: Earth Surface* 114(F3), DOI 10.1029/2008JF001179, f03008

- Cornford SL, Martin DF, Graves DT, Ranken DF, LeBrocq AM, Gladstone RM, Payne AJ, Ng EG, Lipscomb WH (2013) Adaptive mesh, finite volume modeling of marine ice sheets. *J Comput Phys* 232:529–549
- DeConto RM, Pollard D (2003) Rapid Cenozoic glaciation of Antarctica induced by declining atmospheric CO<sub>2</sub>. *Nature* 421:245–249
- DeConto RM, Pollard D (2016) Contribution of Antarctica to past and future sea-level rise. *Nature* 531:591–597, DOI 10.1038/nature17145
- Docquier D, Perichon L, Pattyn F (2011) Representing grounding line dynamics in numerical ice sheet models: Recent advances and outlook. *Surveys in Geophysics* pp 10.1007/s10,712–011–9133–3
- Drews R, Matsuoka K, Martín C, Callens D, Bergeot N, Pattyn F (2015) Evolution of derwael ice rise in dronning maud land, antarctica, over the last millennia. *Journal of Geophysical Research: Earth Surface* 120(3):564–579, DOI 10.1002/2014JF003246, URL <http://dx.doi.org/10.1002/2014JF003246>, 2014JF003246
- Durand G, Gagliardini O, Zwinger T, Le Meur E, Hindmarsh RC (2009) Full stokes modeling of marine ice sheets: influence of the grid size. *Annals of Glaciology* 50(52):109–114, DOI doi:10.3189/172756409789624283
- Favier L, Durand G, Cornford SL, Gudmundsson GH, Gagliardini O, Gillet-Chaulet F, Zwinger T, Payne AJ, Le Brocq AM (2014) "retreat of pine island glacier controlled by marine ice-sheet instability". *Nature Climate Change* 4:117–121
- Fretwell P, Pritchard HD, Vaughan DG, Bamber JL, Barrand NE, Bell R, Bianchi C, Bingham RG, Blankenship DD, Casassa G, Catania G, Callens D, Conway H, Cook AJ, Corr HFJ, Damaske D, Damm V, Ferraccioli F, Forsberg R, Fujita S, Gim Y, Gogineni P, Griggs JA, Hindmarsh RCA, Holmlund P, Holt JW, Jacobel RW, Jenkins A, Jokat W, Jordan T, King EC, Kohler J, Krabill W, Riger-Kusk M, Langley KA, Leitchenkov G, Leuschen C, Luyendyk BP, Matsuoka K, Mouginot J, Nitsche FO, Nogi Y, Nost OA, Popov SV, Rignot E, Rippin DM, Rivera A, Roberts J, Ross N, Siegert MJ, Smith AM, Steinhage D, Studinger M, Sun B, Tinto BK, Welch BC, Wilson D, Young DA, Xiangbin C, Zirizzotti A (2013) Bedmap2: improved ice bed, surface and thickness datasets for antarctica. *The Cryosphere* 7:375–393
- Gillet-Chaulet F, Gagliardini O, Seddik H, Nodet M, Durand G, ritz C, Zwinger T, Greve R, Vaughan D (2012) Greenland Ice Sheet contribution to sea-level rise from a new-generation ice-sheet model. *The Cryosphere Discuss* XX:XXX–XXX
- Hindmarsh RCA (1993) Qualitative dynamics of marine ice sheets. In: Peltier W (ed) *Ice in the Climate System*, Berlin, Springer-Verlag, NATO ASI Series I (12), pp 67–99
- Hindmarsh RCA (1996) Stability of ice rises and uncoupled marine ice sheets. *Ann Glaciol* 23:105–115
- Hindmarsh RCA (2004) A numerical comparison of approximations to the Stokes equations used in ice sheet and glacier modeling. *J Geophys Res* 109(F01012):10.1029/2003JF000,065



- Hindmarsh RCA, Le Meur E (2001) Dynamical processes involved in the retreat of marine ice sheets. *J Glaciol* 47(157):271–282
- Huybrechts P (1990a) A 3-D model for the Antarctic ice sheet: a sensitivity study on the glacial-interglacial contrast. *Climate Dyn* 5:79–92
- Huybrechts P (1990b) The Antarctic ice sheet during the last glacial-interglacial cycle: a 3D model experiment. *Annals of Glaciology* 14:115–119
- Huybrechts P (1992) The Antarctic ice sheet and environmental change: a three-dimensional modelling study. *Berichte für Polarforschung* 99:1–241
- Huybrechts P, Oerlemans J (1990) Response of the Antarctic ice sheet to future greenhouse warming. *Climate Dyn* 5(2):93–102
- Huybrechts P, de Wolde J (1999) The dynamic response of the Greenland and Antarctic ice sheets to multiple-century climatic warming. *Journal of Climate* 12(8):2169–2188
- Huybrechts P, Payne A, The EISMINT Intercomparison Group (1996) The EISMINT benchmarks for testing ice-sheet models. *Ann Glaciol* 23:1–12
- Huybrechts P, Abe-Ouchi A, Marsiat I, Pattyn F, Payne A, Ritz C, Rommelaere V (1998) Report of the Third EISMINT Workshop on Model Intercomparison. European Science Foundation (Strasbourg)
- Joughin I, Smith BE, Medley B (2014) Marine ice sheet collapse potentially under way for the Thwaites glacier basin, West Antarctica. *Science* 344(6185):735–738, DOI 10.1126/science.1249055
- MacAyeal DR (1989) Large-scale ice flow over a viscous basal sediment: Theory and application to Ice Stream B, Antarctica. *J Geophys Res* 94(B4):4071–4087
- MacAyeal DR (1997) *Lessons in Ice-Sheet Modeling*. University of Chicago
- Martin C, Gudmundsson GH, Pritchard HD, Gagliardini O (2009) On the effects of anisotropic rheology on ice flow, internal structure, and the age-depth relationship at ice divides. *Journal of Geophysical Research: Earth Surface* 114(F4):n/a–n/a, DOI 10.1029/2008JF001204, URL <http://dx.doi.org/10.1029/2008JF001204>
- Mercer J (1978) West Antarctic ice sheet and CO<sub>2</sub> greenhouse effect: a threat of disaster. *Nature* 271:321–325
- Morland L (1987) Unconfined ice-shelf flow. In: van der Veen CJ, Oerlemans J (eds) *Dynamics of the West Antarctica Ice Sheet*, Kluwer Acad., Dordrecht, Netherlands, pp 99–116
- Nick FM, Vieli A, Andersen ML, Joughin I, Payne A, Edwards TL, Pattyn F, Van De Wal RSW (2013) Future sea-level rise from Greenland's main outlet glaciers in a warming climate. *Nature* 497(7448):235–238, DOI 10.1038/nature12068

- Pattyn F (2003) A new 3D higher-order thermomechanical ice-sheet model: Basic sensitivity, ice-stream development and ice flow across subglacial lakes. *J Geophys Res* 108(B8, 2382):10.1029/2002JB002,329
- Pattyn F (2017) Sea-level response to melting of antarctic ice shelves on multi-centennial timescales with the fast elementary thermomechanical ice sheet model (f.etish v1.0). *The Cryosphere* 11(4):1851–1878, DOI 10.5194/tc-11-1851-2017, URL <https://www.the-cryosphere.net/11/1851/2017/>
- Pattyn F (2018) The paradigm shift in antarctic ice sheet modelling. *Nature Communications* 9(1):2728, DOI 10.1038/s41467-018-05003-z, URL <https://doi.org/10.1038/s41467-018-05003-z>
- Pattyn F, Huyghe A, De Brabander S, De Smedt B (2006) Role of transition zones in marine ice sheet dynamics. *Journal of Geophysical Research: Earth Surface* 111(F2):n/a–n/a, DOI 10.1029/2005JF000394, f02004
- Pattyn F, Perichon L, Aschwanden A, Breuer B, De Smedt B, Gagliardini O, Gudmundsson GH, Hindmarsh RCA, Hubbard A, Johnson JV, Kleiner T, Konovalov Y, Martin C, Payne AJ, Pollard D, Price S, Rückamp M, Saito F, Soucek O, Sugiyama S, Zwinger T (2008) Benchmark experiments for higher-order and full-Stokes ice sheet models (ISMIP–HOM). *The Cryosphere* 2:95–108
- Pattyn F, Schoof C, Perichon L, Hindmarsh RCA, Bueler E, de Fleurian B, Durand G, Gagliardini O, Gladstone R, Goldberg D, Gudmundsson GH, Huybrechts P, Lee V, Nick FM, Payne AJ, Pollard D, Rybak O, Saito F, Vieli A (2012) Results of the marine ice sheet model intercomparison project, mismip. *The Cryosphere* 6(3):573–588, DOI 10.5194/tc-6-573-2012
- Pattyn F, Perichon L, Durand G, Favier L, Gagliardini O, Hindmarsh RC, Zwinger T, Albrecht T, Cornford S, Docquier D, Fürst JJ, Goldberg D, Gudmundsson GH, Humbert A, Hütten M, Huybrechts P, Jouvett G, Kleiner T, Larour E, Martin D, Morlighem M, Payne AJ, Pollard D, Rückamp M, Rybak O, Seroussi H, Thoma M, Wilkens N (2013) Grounding-line migration in plan-view marine ice-sheet models: results of the ice2sea mismip3d intercomparison. *Journal of Glaciology* 59(215):410–422, DOI 10.3189/2013JoG12J129
- Pattyn F, Favier L, Sun S, Durand G (2017) Progress in numerical modeling of antarctic ice-sheet dynamics. *Current Climate Change Reports* 3(3):174–184, DOI 10.1007/s40641-017-0069-7, URL <https://doi.org/10.1007/s40641-017-0069-7>
- Pollard D, DeConto RM (2009) Modelling West Antarctic ice sheet growth and collapse through the past five million years. *Nature* 458:329–332, DOI 10.1038/nature07809
- Pollard D, DeConto RM (2012) Description of a hybrid ice sheet-shelf model, and application to Antarctica. *Geosci Model Dev* 5:1273–1295, DOI 10.5194/gmd-5-1273-2012
- Pollard D, DeConto RM, Alley RB (2015) Potential antarctic ice sheet retreat driven by hydrofracturing and ice cliff failure. *Earth and Planetary Science Letters* 412:112 – 121
- Raymond CF (1983) Deformation in the vicinity of ice divides. *J Glaciol* 29:357–373

- Reeh N (1989) Parameterization of melt rate and surface temperature on the greenland ice sheet. *Polarforschung* 59(3):113–128
- Rignot E, Mouginot J, Scheuchl B (2011) Ice flow of the antarctic ice sheet. *Science* 333(6048):1427–1430
- Rignot E, Mouginot J, Morlighem M, Seroussi H, Scheuchl B (2014) Widespread, rapid grounding line retreat of pine island, thwaites, smith, and kohler glaciers, west antarctica, from 1992 to 2011. *Geophysical Research Letters* 41(10):3502–3509, DOI 10.1002/2014GL060140
- Rignot EJ (1998) Fast recession of a West Antarctic glacier. *Science* 281(5376):549–551
- Ritz C, Rommelaere V, Dumas C (2001) Modeling the evolution of the Antarctic ice sheet over the last 420000 years: Implications for altitude changes in the Vostok region. *J Geophys Res* 106(D23):31,943–31,964
- Rommelaere V, Ritz C (1996) A thermomechanical model of ice-shelf flow. *Annals of Glaciology* 23:13–20
- Scambos TA, Hulbe C, Fahnestock M, Bohlander J (2000) The link between climate warming and break-up of ice shelves in the antarctic peninsula. *Journal of Glaciology* 46(154):516–530, DOI doi:10.3189/172756500781833043
- Scambos TA, Bohlander JA, Shuman CA, Skvarca P (2004) Glacier acceleration and thinning after ice shelf collapse in the larsen b embayment, antarctica. *Geophysical Research Letters* 31(18):n/a–n/a, DOI 10.1029/2004GL020670, 118402
- Schoof C (2007) Ice sheet grounding line dynamics: Steady states, stability, and hysteresis. *Journal of Geophysical Research: Earth Surface* 112(F3):n/a–n/a, DOI 10.1029/2006JF000664, f03S28
- Schoof C, Hindmarsh R (2010) Thin-film flows with wall slip: an asymptotic analysis of higher order glacier flow models. *Quart J Mech Appl Math* 63(1):73–114
- Seroussi H, Morlighem M, Rignot E, Mouginot J, Larour E, Schodlok M, Khazendar A (2014) Sensitivity of the dynamics of pine island glacier, west antarctica, to climate forcing for the next 50 years. *The Cryosphere* 8(5):1699–1710, DOI 10.5194/tc-8-1699-2014
- Shepherd A, Wingham DJ, Mansley JAD (2002) Inland thinning of the amundsen sea sector, west antarctica. *Geophysical Research Letters* 29(10):2–1–2–4, DOI 10.1029/2001GL014183
- Thomas RH, Bentley CR (1978) A model for Holocene retreat of the West Antarctic Ice Sheet. *Quat Res* 10:150–170
- Tsai VC, Stewart AL, Thompson AF (2015) Marine ice-sheet profiles and stability under coulomb basal conditions. *Journal of Glaciology* 61(226):205–215, DOI doi:10.3189/2015JoG14J221

- Van der Veen CJ, Whillans IM (1989) Force budget: I. theory and numerical methods. *J Glaciol* 35(119):53–60
- Vieli A, Payne AJ (2005) Assessing the ability of numerical ice sheet models to simulate grounding line migration. *Journal of Geophysical Research: Earth Surface* 110(F1):n/a–n/a, DOI 10.1029/2004JF000202, f01003
- Weertman J (1974) Stability of the junction of an ice sheet and an ice shelf. *J Glaciol* 13:3–11
- Wingham DJ, Ridout AJ, Scharroo R, Arthern RJ, Shum CK (1998) Antarctic elevation change from 1992 to 1996. *Science* 282:456–458
- Winkelmann R, Martin MA, Haseloff M, Albrecht T, Bueler E, Khroulev C, Levermann A (2011) The Potsdam Parallel Ice Sheet Model (PISM-PIK) Part 1: Model description. *The Cryosphere* 5:715–726